University of Crete

School of Sciences and Engineering

Department of Materials Science and Technology

Postgraduate Studies Program

‘Moth-eye structures for light trapping in thin organic solar cells’

by

Odysseas Karavanakis

A thesis for the degree of Master of Science

Supervising Professor: D. Papazoglou

OCTOBER 2018

Abstract

In nature, optical structures in the subwavelength range have been evolved over time and serve several purposes. For example, in the form of ‘moth-eye’ structures they show strong antireflective properties on the compound eyes or wings of various species of insects. The bioinspired antireflective structures offer broadband antireflective capabilities to both wavelength and angle because the gradient in the effective refractive index minimizes reflection through index-matching between air and the substrate. So providing antireflection, mostly, in the visible spectrum, is useful for a number of applications. Solar cells, LCD screens and optical lenses are a few examples of applications that can benefit from antireflection. A major issue in organic solar cells is the poor mobility and recombination of the photogenerated charge carriers. The active layer has to be kept thin to facilitate charge transport and minimize recombination losses. However, optical losses due to inefficient light absorption in the thin active layers can be considerable in organic solar cells. Therefore, there is a need for better light trapping in organic solar cells.

In this work, case studies of designing optimized antireflection solutions were carried out. Conventional single layer thin anti-reflective coatings (ARCs) are a simple and low cost solution but only suitable for narrowband applications. A multilayer film stack is often employed for broadband applications. Analytical approaches such as transfer matrix method (TMM) are appropriate for simulation and design of these structures.

More specifically, simulations of the moth-eye design parameters for feature period, height, density factor and shape were carried out. For feature height, it was found that for a height larger than 400nm, the gains in providing antireflection for the visible spectrum are low, so it is not necessary to create features taller than this to achieve a good antireflection performance. For feature fill (density) factor an almost linear monotonic relationship was observed, so for this design parameter, maximization is necessary. For the feature period parameter, it was found that a simple rule could not be extracted and thus to optimize performance, a tailoring of the period for each application has to be done whilst taking into account the incident spectrum.

Περίληψη

Στη φύση, οι οπτικές δομές με διαστάσεις μικρότερες του μήκος κύματος έχουν εξελιχθεί με την πάροδο του χρόνου και εξυπηρετούν διάφορους σκοπούς. Για παράδειγμα, οι δομές ‘moth-eye’, που συναντούμε επί των οφθαλμών ή πτερυγίων διαφόρων ειδών εντόμων, παρουσιάζουν ισχυρές αντι-αντανακλαστικές ιδιότητες. Οι βιομιμητικές αντιανακλαστικές δομές προσφέρουν αντι-αντανακλαστικές δυνατότητες τόσο σε ένα μεγάλο έυρος μήκους κύματος, όσο και στη γωνία πρόσπτωσης, διότι δημιουργούν ένα μέσο μεταβλητού δείκτη διάθλασης, ελαχιστοποιώντας τη διαφορά του δείκτη διάθλασης μεταξύ αέρα και υποστρώματος. Έτσι, οι αντι-ανακλαστικές ιδιότητες, κυρίως στο ορατό φάσμα, είναι χρήσιμες για πολλές εφαρμογές. Τα φωτοβολταικά, οι οθόνες LCD και οι οπτικοί φακοί είναι μερικά παραδείγματα εφαρμογών που μπορούν να επωφεληθούν από τέτοιες ιδιότητες.

Στη συγκεκριμένη εργασία, διεξήχθη μελέτη ώστε να διερευνηθούν βέλτιστες λύσεις για το σχεδιασμό αντι-ανακλαστικών επιφανειών. Τα συμβατικά μονοστρωματικά αντι-αντανακλαστικά επιστρώματα είναι μια απλή, και χαμηλού κόστους, λύση αλλά είναι κατάλληλα μόνο για εφαρμογές που στοχεύουν σε συγκεκριμένο μήκος κύματος. Για εφαρμοργές που μας ενδιαφέρει μεγαλύτερο εύρος του μήκους κύματος, συχνά χρησιμοποιούνται πολυστρωματικά αντιανακλαστικά επιστρώματα. Για την προσομοίωση και το σχεδιασμό αυτών των δομών, κατάλληλες είναι οι αναλυτικές μέθοδοι επίλυσης όπως η μέθοδος μεταφοράς πίνακα (TMM).

Πιο συγκεκριμένα, έγιναν προσομοιώσεις των παραμέτρων σχεδίασης των δομών ‘moth-eye’ ως προς τα γεωμετρικά χαρακτηριστικά όπως η περίοδος, το ύψος, ο συντελεστής πλήρωσης και το σχήμα. Ως προς το ύψος των δομών, διαπιστώθηκε ότι για ύψος μεγαλύτερο από 400 nm, η μείωση της ανακλαστικότητας για το ορατό φάσμα είναι μικρή, οπότε δεν είναι απαραίτητο να δημιουργηθούν πιο ψηλές δομές ώστε να επιτευχθεί καλή αντι-ανακλαστικότητα. Ως προς το συντελεστή πλήρωσης, παρατηρήθηκε μια σχεδόν γραμμική σχέση μείωσης της ανακλαστικότας με την αύξηση του συντελεστή πλήρωσης της επιφάνειας, οπότε η μεγιστοποίησή του κρίνεται απαραίτητη. Όσον αφορά την περιόδο των δομών, διαπιστώθηκε ότι δεν ήταν δυνατή η εξαγωγή ενός απλού κανόνα και, συνεπώς, για τη βελτιστοποίηση της απόδοσης, πρέπει να γίνει προσαρμογή της περιόδου για κάθε εφαρμογή λαμβάνοντας υπόψη το φάσμα μήκους κύματος.

Acknowledgments

A lot of people, in one way or the other, have helped me reach a point where I could successfully propose, work on, write, and defend this Master's thesis.

First and foremost, I would like to express my sincere appreciation and gratitude to my supervisor Prof. Dimitris Papazoglou who has supported me the last couple of years. I feel very fortunate to have been under his guidance, including his supervision of my Optics courses. I believe I have learned a lot being his student and I think his patience, and unending support through my entire dissertation process made it possible for me that I managed to finish in time.

I would like to thank my parents, Nikos and Christoula, and my sister, Argyro, for their endless love and support. The biggest reason for my success today is all of their hard work and sacrifices that they have made for me. I would also like to thank all of my friends for their patience and support, during difficult times.

Finally, I would like to thank my internal and external examiners, Dr. Emmanuel Stratakis and Dr. Maria Kafesaki for their very useful comments and for assisting greatly in shaping the final version of this thesis.

Contents

1 Chapter 1 – Introduction

1.1 Overview of dissertation

Organic solar cells have received a great deal of attention over the years, largely due to increasing performance and advances in fabrication technologies. To this day, fabrication and optical behavior remain decoupled during the design phase as the main research focuses on material selection. So the study in the optical characteristics of these devices plays a key role in order to improve performance. In order to minimize optical losses related to reflection we need to find optimal solutions such as thin-film anti-reflection coating or structures. The anti-reflection research is needed not only in the field of photovoltaics, but can be extended in a really wide range of applications.

This dissertation focuses into two main anti-reflection categories, thin-film coatings and biomimetic subwavelength structures. For the first case, a numerical tool was developed in Maxima from scratch to model thin-film anti-reflection coatings. The simulations include single-, double- and multi-layer systems but also there is the capability to simulate nearly any system that is based on thin-film layers, i.e. Bragg reflectors. For the second case, the study focuses on biomimetic subwavelength anti-reflection structures which can be found on the eyes and wings of several species of insects. In order to conduct optical simulations for these types of structures, was used a commercially available software from Lumerical Inc. The FDTD Solutions is a capable tool which is based on the finite-difference time-domain (FDTD) method to model optical performance of the simulated structures. Using this tool, subwavelength elements were designed and optimized with regard to their optical behavior.

1.2 Outline of dissertation

Chapter 1 introduces the topic of this thesis. The concept of subwavelength anti-reflection structures (SWARS) is presented and the importance of modeling the different design characteristics is illustrated.

Chapter 2 describes numerical tools used to model thin-film anti-reflection coatings, in particular a script that was developed in Maxima and the main electromagnetic simulation tools used in this dissertation which is FDTD.

Chapter 3 contains the simulation results of reflectivity of thin-film anti-reflective coatings obtained from Maxima (TMM). The study involves single, double and triple anti-reflective coatings as long as multilayer periodic systems.

Chapter 4 contains the FDTD simulation results of reflectivity of the subwavelength biomimetic structures. At first, a comparative validation between reference and simulation results was conducted. Then, using a cicada wing bio-template, morphological and topographical specifications of the protuberances were studied. Finally, a thin organic solar cell that utilizes this type of structure was studied with regard to its reflectance.

Chapter 5 summarizes the dissertation and reviews key developments achieved in this work.

2 Chapter 2 – Literature review

2.1 Optics background

2.1.1 Propagation of light

The speed of a wave depends upon the medium in which it propagates. In particular, the speed of light in a medium is less than in vacuum, which means that the same frequency will correspond to a shorter wavelength in the medium than in vacuum.

This change in speed upon entering a medium causes refraction, or a change in direction of waves that encounter the interface between media at an angle. For electromagnetic waves, this change in the angle of propagation is governed by Snell's law

$$\frac{n_1}{n_2} = \frac{\sin\theta_1}{\sin\theta_2} \tag{1}$$

where θ_1 and θ_2 are the angles of incidence and refraction, respectively, of a ray crossing the interface between two media with refractive indices n_1 and n_2.

The wave velocity in one medium not only may differ from that in another, but the velocity typically varies with wavelength. As a result, the change in direction upon entering a different medium, changes, with the wavelength of the wave.

For electromagnetic waves the speed in a medium is governed by its refractive index according to

$$u = \frac{c}{n(\lambda_0)} \tag{2}$$

where c is the speed of light in vacuum and $n(\lambda_0)$ is the refractive index of the medium at wavelength λ_0, where the latter is measured in vacuum rather than in the medium. The corresponding wavelength in the medium is

$$\lambda = \frac{\lambda_0}{n(\lambda_0)} \tag{3}$$

When wavelengths of electromagnetic radiation are quoted, the wavelength in vacuum usually is intended unless the wavelength is specifically identified as the wavelength in some other medium. In acoustics, where a medium is essential for the waves to exist, the wavelength value is given for a specified medium.

As it's already mentioned, when light moves from one medium to another, it changes direction, i.e. it is refracted. When light enters a material with higher refractive index, the angle of refraction will be smaller than the angle of incidence and the light will be refracted towards the normal of the surface. The higher the refractive index, the closer to the normal direction the light will travel. When passing into a medium with lower refractive index, the light will instead be refracted away from the normal, towards the surface.

While the refractive index affects wavelength, it depends on photon frequency, color and energy so the resulting difference in the bending angle causes white light to split into its constituent colors. This is called dispersion. It can be observed in prisms and rainbows, and chromatic aberration in lenses. Light propagation in absorbing materials can be described using a complex-valued refractive index. The imaginary part then handles the attenuation, while the real part accounts for refraction.

Apart from the transmitted light there is also a reflected part. The reflection angle is equal to the incidence angle, and the amount of light that is reflected is determined by the reflectivity of the surface. The reflectivity can be calculated from the refractive index and the incidence angle with the Fresnel equations, which for normal incidence reduces to

$$R = \left(\frac{n_1 - n_2}{n_1 + n_2}\right)^2 \tag{4}$$

For common glass in air, n_1 = 1 and n_2 = 1.5, and thus about 4% of the incident power is reflected.

2.1.2 Electromagnetic approach

The electromagnetic theory of optics begins with Maxwell's equations. In, fact the electromagnetic theory forms a complete theory of optical propagation phenomena, capable of describing most of the known observation on the propagation of light. [1]

2.1.2.1 Maxwell's equations

The intent of this section is to review and develop some of the ideas needed to appreciate the concept of electromagnetic waves. As we'll see, electric fields are generated by both electric charges and time-varying magnetic fields. Similarly, magnetic fields are generated by electric currents and by time-varying electric fields. This interdependence of $\vec{E}$ and $\vec{B}$ is a key point in the description of light.

- **Faraday's Induction Law**

"Convert magnetism into electricity" was the brief remark Michael Faraday jotted in his notebook in 1822. Using a ferromagnetic core to concentrate the "magnetic force", Faraday wound two coils around opposing sections of a soft iron ring. The effect was that the changing magnetic field generated a current. By thrusting a magnet into a coil, Faraday showed that there is a voltage (otherwise known as the induced electromotive force or emf) across the coil's terminals. When the same changing B-field passes through two different wire loops, the induced emf is proportional to the area A of the loop penetrated perpendicularly by the field and when the field is constant, the induced emf is proportional to the rate of change of the perpendicular area penetrated.

All of this suggests that the emf depends on the rate of change of both $A_{\perp}$, and B, that is on the rate of change of their product. Accordingly, the flux of the magnetic field through the wire loop is

$$\Phi_M = B_{\perp} A = A_{\perp} B = BA\cos\theta \tag{5}$$

More generally, if B varies in space as it's likely to, the flux of the magnetic field through any open area A bounded by the conducting loop is given by

$$\Phi_M = \iint_A \vec{B} \cdot d\vec{S} \tag{6}$$

The induced emf, developed around the loop, is then

$$emf = -\frac{d\Phi_M}{dt} \tag{7}$$

In very general terms, an emf is a potential difference, and that's a potential-energy difference per unit charge. The emf exists only as a result of the presence of an electric field

$$emf = \oint_C \vec{E} \cdot d\vec{l} \tag{8}$$

Finally we get

$$\oint_C \vec{E} \cdot d\vec{l} = -\frac{d}{dt} \iint_A \vec{B} \cdot d\vec{S} \tag{9}$$

We are interested in electromagnetic waves traveling in space where there are no wire loops, and the magnetic flux changes because $\vec{B}$ changes. The induction law can then be rewritten as

$$\oint_C \vec{E} \cdot d\vec{l} = -\iint_A \frac{\partial \vec{B}}{\partial t} \cdot d\vec{S} \tag{10}$$

- **Gauss's Law – Electric**

Gauss's Law is about the relationship between the flux of the electric field and the sources of that flux, charge. The discharge rate, or volume flux (Av), is the volume of fluid flowing past a point in the tube per unit time. The volume flux through both end surfaces is equal in magnitude - what flows in per second flows out per second. The net fluid flux (into and out of the closed area) summed over all the surfaces equals zero. To apply these ideas to the electric field, consider an imaginary closed area A placed in some arbitrary electric field. The flux of electric field through A is taken to be

$$\Phi_E = \oiint_A \vec{E} \cdot d\vec{S} \tag{11}$$

The circled double integral serves as a reminder that the surface is closed. The vector dS is in the direction of an outward normal. When there are no sources or sinks of the electric field within the region encompassed by the closed surface, the net flux through the surface equals zero. Consider a spherical surface of radius r centered on and surrounding a positive point-charge (q) in the vacuum. The E-field is everywhere outwardly radial, and at any distance r it is entirely perpendicular to the surface, $E = E_{\perp}$. Since E is constant over the surface of the sphere, it can be taken out of the integral and as we know from Coulomb's Law we get Gauss's Law

$$\oiint_A \vec{E} \cdot d\vec{S} = \frac{1}{\varepsilon_0} \sum q \tag{12}$$

- **Gauss's Law – Magnetic**

Unlike the electric field, the magnetic field B does not diverge from or converge toward some kind of magnetic charge. Magnetic fields can be described in terms of current distributions. Indeed, we might envision an elementary magnet as a small current loop in which the lines of B, are continuous and closed. Any closed surface in a region of magnetic field would accordingly have an equal number of lines of B entering and emerging from it. This situation arises from the absence of any monopoles within the enclosed volume.

The flux of magnetic field Φ_M, through such a surface is zero, and we have the magnetic equivalent of Gauss's Law

$$\Phi_M = \oiint_A \vec{B} \cdot d\vec{S} = 0 \tag{13}$$

- **Ampere's Law**

Suppose we carry a north-seeking monopole around a closed circular path perpendicular to and centered on a current-carrying wire and determine the work done in the process. Since the direction of the force changes, because B changes direction, we will have to divide the circular path into tiny segments (Δl) and sum up the work-k done over each. With both q_m and *R* constant, the summation becomes

$$q_m \sum B_{\|} \Delta \ell = q_m B \sum \Delta \ell = q_m B 2\pi r \tag{14}$$

Since no work is done in traveling perpendicular to B, the work must be the same if we move q_m along a radius, carrying it from one circular segment to another as we go around. Putting in the current expression for R and canceling the "charge" q_m we get the rather remarkable expression

$$\sum B_{\|} \Delta \ell = \mu_0 i \tag{15}$$

which is to be summed over any closed path surrounding i.

If there are several current-carrying wires encompassed by the closed path, their fields will superimpose and add, yielding a net field. As $\Delta l \rightarrow 0$, the sum becomes an integral around a closed path

$$\oint_C \vec{B} \cdot d\vec{\ell} = \mu_0 \sum i \tag{16}$$

This equation is known as the Ampere's Law and it relates a line integral of B tangent to a closed curve C, with the total current i passing within the confines of C.

When the current has a non-uniform cross section, Ampere's Law is written in terms of the current density or current per unit area J, integrated over the area

$$\oint_C \vec{B} \cdot d\vec{\ell} = \mu_0 \iint_A \vec{J} \cdot d\vec{S} \tag{17}$$

The restatement of Ampere's Law as

$$\oint_C \vec{B} \cdot d\vec{\ell} = \mu \iint_A \left(\vec{J} + \varepsilon \frac{\partial \vec{E}}{\partial t} \right) \cdot d\vec{S} \tag{18}$$

was one of Maxwell's greatest contributions. It points out that even when J = 0, a time-varying E-field will be accompanied by a B-field.

2.1.2.2 Waves at an interface

The incident light is a plane wave:

$$\mathbf{E}_i = \mathbf{E}_{0i} \exp[i(\mathbf{k}_i \cdot \mathbf{r} - \omega_i t)] \tag{19}$$

or, more simply,

$$\mathbf{E}_i = \mathbf{E}_{0i} \cos(\mathbf{k}_i \cdot \mathbf{r} - \omega_i t) \tag{20}$$

Reflected and transmitted waves:

$$\mathbf{E}_r = \mathbf{E}_{0r} \cos(\mathbf{k}_r \cdot \mathbf{r} - \omega_r t + \varepsilon_r) \tag{21}$$

and

$$\mathbf{E}_t = \mathbf{E}_{0t} \cos(\mathbf{k}_t \cdot \mathbf{r} - \omega_t t + \varepsilon_t) \tag{22}$$

where ε_r and ε_t are phase constants relative to $\mathbf{E}_i$.

The laws of electromagnetic theory lead to certain requirements that must be met by the fields, and these are referred to as the boundary conditions. The total tangential component of **E** on one side of the surface must equal that on the other. Hence:

$$\hat{u}_n \times \mathbf{E}_i + \hat{u}_n \times \mathbf{E}_r = \hat{u}_n \times \mathbf{E}_t \tag{23}$$

or

$$\hat{u}_n \times \mathbf{E}_{0i} \cos(\mathbf{k}_i \cdot \mathbf{r} - \omega_i t) + \hat{u}_n \times \mathbf{E}_{0r} \cos(\mathbf{k}_r \cdot \mathbf{r} - \omega_r t) = \hat{u}_n \times \mathbf{E}_{0t} \cos(\mathbf{k}_t \cdot \mathbf{r} - \omega_t t) \tag{24}$$

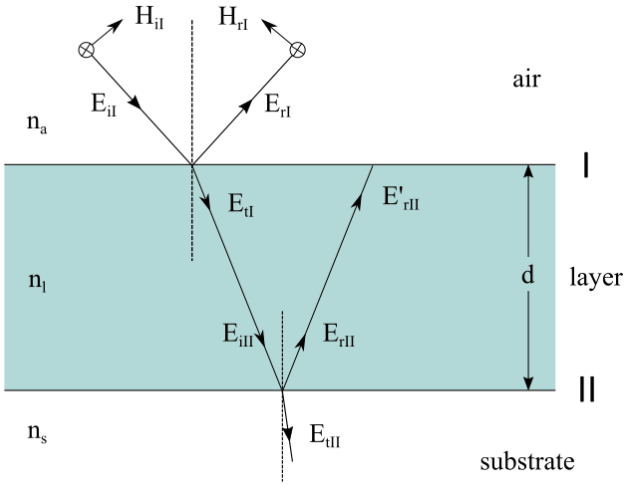

Figure 1: Fields at the boundaries

This relationship must obtain at any instant in time and at any point on the interface ($y=b$), which means that $\mathbf{E}_i$, $\mathbf{E}_r$ and $\mathbf{E}_t$ must have the same the same functional dependence on r and t:

$$(\mathbf{k}_i \cdot \mathbf{r} - \omega_i t)\big|_{y=b} = (\mathbf{k}_r \cdot \mathbf{r} - \omega_r t + \varepsilon_r)\big|_{y=b} = (\mathbf{k}_t \cdot \mathbf{r} - \omega_t t + \varepsilon_t)\big|_{y=b} \tag{25}$$

As this has to be true for all values of time, the coefficients of t must be equal:

$$\omega_i = \omega_r = \omega_t \tag{26}$$

Whatever light is scattered has that same frequency:

$$(\mathbf{k}_i \cdot \mathbf{r})\big|_{y=b} = (\mathbf{k}_r \cdot \mathbf{r} + \varepsilon_r)\big|_{y=b} = (\mathbf{k}_t \cdot \mathbf{r} + \varepsilon_t)\big|_{y=b} \tag{27}$$

wherein ***r*** terminates on the interface.

From the first two terms we obtain:

$$\left[(\mathbf{k}_i - \mathbf{k}_r) \cdot \mathbf{r}\right]_{y=b} = \varepsilon_r \tag{28}$$

This says that the endpoint of **r** sweeps out a plane (interface) perpendicular to the vector $(\mathbf{k}_i - \mathbf{k}_r)$ or parallel to $\hat{u}_n$. However, since the incident and the reflected waves are in the same medium, $\mathbf{k}_i = \mathbf{k}_r$. We conclude that:

$$k_i \sin\theta_i = k_r \sin\theta_r \tag{29}$$

hence we have the law of reflection, that is,

$$\theta_i = \theta_r \tag{30}$$

Furthermore, since $(\mathbf{k}_i - \mathbf{k}_r)$ is parallel to $\hat{u}_n$ all three vectors, $\mathbf{k}_i$, $\mathbf{k}_r$, and $\hat{u}_n$ are in the same plane, the plane of incidence:

$$\left[(\mathbf{k}_i - \mathbf{k}_t) \cdot \mathbf{r}\right]_{y=b} = \varepsilon_t \tag{31}$$

Thus $\mathbf{k}_i$, $\mathbf{k}_r$, $\mathbf{k}_t$ and $\hat{u}_n$ are all coplanar. As before, the tangential components $\mathbf{k}_i$ and $\mathbf{k}_t$ must be equal and consequently:

$$k_i \sin\theta_i = k_t \sin\theta_t \tag{32}$$

But because $\omega_i = \omega_t$, we can multiply both sides by c / ω_i to get:

$$n_i \sin\theta_i = n_t \sin\theta_t \tag{33}$$

which is the Snell's law.

2.1.2.3 Derivation of the Fresnel equations

The Fresnel equations relate the amplitudes, phases, and polarizations of the transmitted and reflected waves that emerge when light enters an interface between two transparent media with different indices of refraction, to the corresponding parameters of the incident waves. These equations were derived by Augustin-Jean Fresnel in 1823 as a part of his comprehensive wave theory of light. However, the Fresnel equations are fully consistent with the rigorous treatment of light in the framework of Maxwell equations. The Fresnel equations are among the most fundamental findings of classical optics. Because they describe the behavior of light at optical surfaces, they are relevant to virtually all fields of optical design: lens design, imaging, lasers, optical communication, spectroscopy, and holography. Good understanding of the principles behind Fresnel equations is necessary in designing optical coatings. [1]

- **E perpendicular to the plane of incidence (TE)**

We assume that **E** is perpendicular to the plane of incidence and that **B** is parallel to it. Recall that $E = uB$, so that:

$$\hat{k} \times E = uB \tag{34}$$

and

$$\hat{k} \cdot E = 0 \tag{35}$$

We have at the boundary at any time and any point:

$$\mathbf{E}_{0i} + \mathbf{E}_{0r} = \mathbf{E}_{0t} \tag{36}$$

We will need to invoke another of the boundary conditions in order to get one more equation. Although the tangential component of **E** is continuous across the boundary, its normal component is not. Instead the normal component of the product e**E** is the same on either side of the interface. Similarly, the normal component of **B** is continuous, as is the tangential component of $\mu^{-1}\mathbf{B}$.

$$-\frac{B_i}{\mu_i}\cos\theta_i + \frac{B_r}{\mu_r}\cos\theta_r = -\frac{B_t}{\mu_t}\cos\theta_t \tag{37}$$

From $\hat{k}\times E = uB$ we have:

$$B_i = E_i/\mathrm{u}_i \tag{38}$$

$$B_r = E_r/\mathrm{u}_r \tag{39}$$

and

$$B_t = E_t/\mathrm{u}_t \tag{40}$$

Thus since $u_i = u_r$ and $\theta_i = \theta_r$ we can write:

$$\frac{1}{\mu_i u_i}(E_i - E_r)\cos\theta_i = \frac{1}{\mu_t u_t}E_t\cos\theta_t \tag{41}$$

Remembering that the cosines therein equal one another $y = 0$, we obtain:

$$\frac{n_i}{\mu_i}(E_{0i} - E_{0r})\cos\theta_i = \frac{n_t}{\mu_t}E_{0t}\cos\theta_t \tag{42}$$

Combined with the boundary equation, this yields

$$\left(\frac{E_{0r}}{E_{0i}}\right)_{\perp} = \frac{\frac{n_i}{\mu_i}\cos\theta_i - \frac{n_t}{\mu_t}\cos\theta_t}{\frac{n_i}{\mu_i}\cos\theta_i + \frac{n_t}{\mu_t}\cos\theta_t} \tag{43}$$

and

$$\left(\frac{E_{0t}}{E_{0i}}\right)_{\perp} = \frac{2\frac{n_i}{\mu_i}\cos\theta_i}{\frac{n_i}{\mu_i}\cos\theta_i + \frac{n_t}{\mu_t}\cos\theta_t} \tag{44}$$

For $\mu_i \approx \mu_t \approx \mu_0$:

$$r_{\perp} \equiv \left(\frac{E_{0r}}{E_{0i}}\right)_{\perp} = \frac{n_i\cos\theta_i - n_t\cos\theta_t}{n_i\cos\theta_i + n_t\cos\theta_t} \tag{45}$$

and

$$t_{\perp} \equiv \left(\frac{E_{0t}}{E_{0i}}\right)_{\perp} = \frac{2n_i\cos\theta_i}{n_i\cos\theta_i + n_t\cos\theta_t} \tag{46}$$

Here $r_{\perp}$ denotes the amplitude reflection coefficient and $t_{\perp}$ the amplitude transmission coefficient and are two of the Fresnel equations.

- **E parallel to the plane of incidence (TM)**

Continuity of the tangential components of **E** on either side of the boundary leads to:

$$E_{0i}\cos\theta_i - E_{0r}\cos\theta_r = E_{0t}\cos\theta_t \tag{47}$$

In the same way as before, continuity of the tangential components of B/μ yields:

$$\frac{1}{\mu_i u_i}E_{0i} + \frac{1}{\mu_r u_r}E_{0r} = \frac{1}{\mu_t u_t}E_{0t} \tag{48}$$

Using the fact that $\mu_i = \mu_r$ and $\theta_i = \theta_r$, we can combine these formulas to obtain two more of the Fresnel equations:

$$\left(\frac{E_{0r}}{E_{0i}}\right)_{\parallel} = \frac{\frac{n_t}{\mu_t}\cos\theta_i - \frac{n_i}{\mu_i}\cos\theta_t}{\frac{n_i}{\mu_i}\cos\theta_t + \frac{n_t}{\mu_t}\cos\theta_i} \tag{49}$$

and

$$\left(\frac{E_{0t}}{E_{0i}}\right)_{\|} = \frac{2\frac{n_i}{\mu_i}\cos\theta_i}{\frac{n_i}{\mu_i}\cos\theta_t + \frac{n_t}{\mu_t}\cos\theta_i} \tag{50}$$

When both media forming the interface are dielectrics, the amplitude coefficients become:

$$r_{\|} \equiv \left(\frac{E_{0r}}{E_{0i}}\right)_{\|} = \frac{n_t\cos\theta_i - n_i\cos\theta_t}{n_i\cos\theta_t + n_t\cos\theta_i} \tag{51}$$

and

$$t_{\|} \equiv \left(\frac{E_{0t}}{E_{0i}}\right)_{\|} = \frac{2n_i\cos\theta_i}{n_i\cos\theta_t + n_t\cos\theta_i} \tag{52}$$

2.1.2.4 Transfer Matrix Method (TMM)

The boundary conditions require that the tangential components of both the electric (**E**) and the magnetic ($\mathbf{H} = \mathbf{B}/\mu$) fields be continuous across the boundaries (equal on both sides).

At the boundary I:

$$E_I = E_{iI} + E_{rI} = E_{tI} + E'_{rII} \tag{53}$$

and

$$H_I = \sqrt{\frac{\varepsilon_0}{\mu_0}}\left(E_{iI} - E_{rI}\right)n_0\cos\theta_{iI} \tag{54}$$

$$H_I = \sqrt{\frac{\varepsilon_0}{\mu_0}}\left(E_{tI} - E'_{rII}\right)n_1\cos\theta_{iII} \tag{55}$$

where use is made of the fact that E and H in non-magnetic media are related through the index of refraction and the unit propagation vector:

$$\mathbf{H} = \sqrt{\frac{\varepsilon_0}{\mu_0}}n\hat{\mathbf{k}}\times\mathbf{E} \tag{56}$$

At the boundary II:

$$E_{II} = E_{iII} + E_{rII} = E_{tII} \tag{57}$$

and

$$H_{II} = \sqrt{\frac{\varepsilon_0}{\mu_0}} \left(E_{iII} - E_{rII} \right) n_1 \cos\theta_{iII} \tag{58}$$

$$H_{II} = \sqrt{\frac{\varepsilon_0}{\mu_0}} E_{tII} n_s \cos\theta_{tII} \tag{59}$$

the substrate having an index n_s. A wave that traverses the film, undergoes a shift in phase of $k_0 \left(2 n_1 d \cos\theta_{iII} \right) / 2$ which will be denoted by $k_0 h$, so that:

$$E_{iII} = E_{tI} e^{-ik_0 h} \tag{60}$$

and

$$E_{rII} = E'_{rII} e^{+ik_0 h} \tag{61}$$

Equations at boundary II can now be written as:

$$E_{II} = E_{tI} e^{-ik_0 h} + E'_{rII} e^{+ik_0 h} \tag{62}$$

and

$$H_{II} = \left(E_{tI} e^{-ik_0 h} - E'_{rII} e^{+ik_0 h} \right) \sqrt{\frac{\varepsilon_0}{\mu_0}} n_1 \cos\theta_{iII} \tag{63}$$

These last two equations can be solved for E_{tI} and E'_{rII}, which when substituted into the boundary I equations yield:

$$E_I = E_{II} \cos k_0 h + H_{II} \left(i \sin k_0 h \right) / Y_1 \tag{64}$$

and

$$H_I = E_{II} Y_1 i \sin k_0 h + H_{II} \cos k_0 h \tag{65}$$

where

$$Y_1 \equiv \sqrt{\frac{\varepsilon_0}{\mu_0}} n_1 \cos\theta_{iII} \tag{66}$$

When **E** is in the plane of incidence, the above calculations result in similar equations, provided that now:

$$Y_1 \equiv \sqrt{\frac{\varepsilon_0}{\mu_0}}\, n_1 / \cos\theta_{iII} \tag{67}$$

In matrix notation, the above linear relations take the form:

$$\begin{pmatrix} E_I \\ H_I \end{pmatrix} = \begin{pmatrix} \cos k_0 h & \left(i \sin k_0 h\right)/Y_1 \\ Y_1 i \sin k_0 h & \cos k_0 h \end{pmatrix} \begin{pmatrix} E_{II} \\ H_{II} \end{pmatrix} \tag{68}$$

or

$$\begin{pmatrix} E_I \\ H_I \end{pmatrix} = \mathbf{M}_I \begin{pmatrix} E_{II} \\ H_{II} \end{pmatrix} \tag{69}$$

The characteristic matrix $\mathbf{M}_\mathrm{I}$ relates the fields at the two adjacent boundaries. If two overlaying films are deposited on the substrate, there will be three boundaries (interfaces) and now:

$$\begin{pmatrix} E_{II} \\ H_{II} \end{pmatrix} = \mathbf{M}_{II} \begin{pmatrix} E_{III} \\ H_{III} \end{pmatrix} \tag{70}$$

Multiplying both sides by $\mathbf{M}_\mathrm{I}$ we obtain:

$$\begin{pmatrix} E_I \\ H_I \end{pmatrix} = \mathbf{M}_I \mathbf{M}_{II} \begin{pmatrix} E_{III} \\ H_{III} \end{pmatrix} \tag{71}$$

If p is the number of layers, the first and the last boundaries are related by

$$\begin{pmatrix} E_I \\ H_I \end{pmatrix} = \mathbf{M}_I \mathbf{M}_{II} \cdots \mathbf{M}_p \begin{pmatrix} E_{(p+1)} \\ H_{(p+1)} \end{pmatrix} \tag{72}$$

The characteristic matrix of the entire system is the resultant of the product of the individual 2x2 matrices, that is:

$$\mathbf{M} = \mathbf{M}_I \mathbf{M}_{II} \cdots \mathbf{M}_p = \begin{pmatrix} m_{11} & m_{12} \\ m_{21} & m_{22} \end{pmatrix} \tag{73}$$

To see how all this fit together, we will derive expressions for the amplitude coefficients of reflection and transmission using the above scheme. By reformulating Eq. in terms of the boundary conditions and setting:

$$Y_0 \equiv \sqrt{\frac{\varepsilon_0}{\mu_0}} n_0 \cos\theta_{iI} \tag{74}$$

and

$$Y_s \equiv \sqrt{\frac{\varepsilon_0}{\mu_0}} n_s \cos\theta_{tII} \tag{75}$$

we obtain:

$$\begin{pmatrix} E_{iI} + E_{rI} \\ \left(E_{iI} - E_{rI}\right) Y_0 \end{pmatrix} = \mathbf{M}_1 \begin{pmatrix} E_{tII} \\ E_{tII} Y_s \end{pmatrix} \tag{76}$$

When the matrices are expanded, the last relation becomes:

$$1 + r = m_{11} t + m_{12} Y_s t \tag{77}$$

and

$$\left(1 - r\right) Y_0 = m_{21} t + m_{22} Y_s t \tag{78}$$

inasmuch as:

$$r = E_{rI} / E_{iI} \tag{79}$$

and

$$t = E_{tII} / E_{iI} \tag{80}$$

Consequently:

$$r = \frac{Y_0 m_{11} + Y_0 Y_s m_{12} - m_{21} - Y_s m_{22}}{Y_0 m_{11} + Y_0 Y_s m_{12} + m_{21} + Y_s m_{22}} \tag{81}$$

and

$$t = \frac{2Y_0}{Y_0 m_{11} + Y_0 Y_s m_{12} + m_{21} + Y_s m_{22}} \tag{82}$$

To find either *r* or *t* for any configuration of films, we need only to compute the characteristic matrices for each film, multiply them, and then substitute the resulting matrix elements into the above equations.

2.1.2.5 Antireflection coatings

Now consider the extremely important case of normal incidence, that is:

$$\theta_{iI} = \theta_{iII} = \theta_{tII} = 0 \tag{83}$$

If we put a subscript on *r* to indicate the number of layers present, the reflection coefficient for a single film becomes:

$$r_1 = \frac{n_1 \left(n_0 - n_s \right) \cos k_0 h + i \left(n_0 n_s - n_1^2 \right) \sin k_0 h}{n_1 \left(n_0 + n_s \right) \cos k_0 h + i \left(n_0 n_s + n_1^2 \right) \sin k_0 h} \tag{84}$$

Multiplying r_1 by its complex conjugate leads to the reflectance:

$$R_1 = \frac{n_1^2 \left(n_0 - n_s \right)^2 \cos^2 k_0 h + \left(n_0 n_s - n_1^2 \right)^2 \sin^2 k_0 h}{n_1^2 \left(n_0 + n_s \right)^2 \cos^2 k_0 h + \left(n_0 n_s + n_1^2 \right)^2 \sin^2 k_0 h} \tag{85}$$

This formula becomes particularly simple when $k_0 h = \frac{1}{2}\pi$, which is equivalent to saying that the optical thickness *h* of the film is an odd multiple of $\frac{1}{4}\lambda_0$. In this case $d = \frac{1}{4}\lambda_f$, and:

$$R_1 = \frac{\left(n_0 n_s - n_1^2\right)^2}{\left(n_0 n_s + n_1^2\right)^2} \tag{86}$$

which, quite remarkably, will equal zero when:

$$n_1^2 = n_0 n_s \tag{87}$$

For a double-layer, quarter-wavelength antireflection coating:

$$\mathbf{M} = \mathbf{M}_I \mathbf{M}_{II} \tag{88}$$

or more specifically

$$\mathbf{M} = \begin{pmatrix} 0 & i/Y_1 \\ iY_1 & 0 \end{pmatrix} \begin{pmatrix} 0 & i/Y_2 \\ iY_2 & 0 \end{pmatrix} \tag{89}$$

At normal incidence this becomes:

$$\mathbf{M} = \begin{pmatrix} -n_2/n_1 & 0 \\ 0 & -n_1/n_2 \end{pmatrix} \tag{90}$$

Substituting the appropriate matrix elements into Eq. yields r_2, which when squared, leads to the reflectance:

$$R_2 = \left(\frac{n_2^2 n_0 - n_s n_1^2}{n_2^2 n_0 + n_s n_1^2} \right)^2 \tag{91}$$

For R_2 to be exactly zero at a particular wavelength, we need:

$$\left(\frac{n_2}{n_1} \right)^2 = \frac{n_s}{n_0} \tag{92}$$

This kind of film is referred to as a double-quarter, single-minimum coating. When n_1 and n_2 are as small as possible, the reflectance will have its single broadest minimum equal to zero at the chosen frequency.

2.2 About photovoltaics (PVs)

2.2.1 Basic principle

There are various types of solar cells. However, the most basic and common type is the simple silicon semiconductor P-N diode. First generation solar cells are made out of these P-N diodes; a combination of P-doped and N-doped single crystal silicon with electrical contacts present at either side of the diode.

Sunlight enters the solar cell in the form of photons (Figure 2). If the energy of the photon is higher or equal to the band gap energy between the valence and the conduction band of the semiconductor and the thickness of the cell is enough to allow significant absorption at that wavelength, it has a good chance of being absorbed by an electron in the silicon lattice. When a photon with enough energy is absorbed by an electron in the silicon lattice it is excited from the valence to the conduction band, and thus becomes unbound from the silicon atom and is free to move within the crystal lattice. The in-built inherit electrical field that exists in the space charge region accelerates the electron and allows it to drift across the PN junction. It then becomes a majority charge carrier in the N type region before being collected by the metal contacts. The opposite occurs for the ’hole particle’ which is the positively charged particle that accounts for the absence of an electron from the lattice, it drifts across the PN junction and travels through the P type material to the metal contact. This effect produces current which, combined to the voltage created by the inherit field across the P-N junction provides electrical power. If the photon that enters the cell has energy which is smaller than the band gap of the material, then it is not absorbed by the device and passes through it.

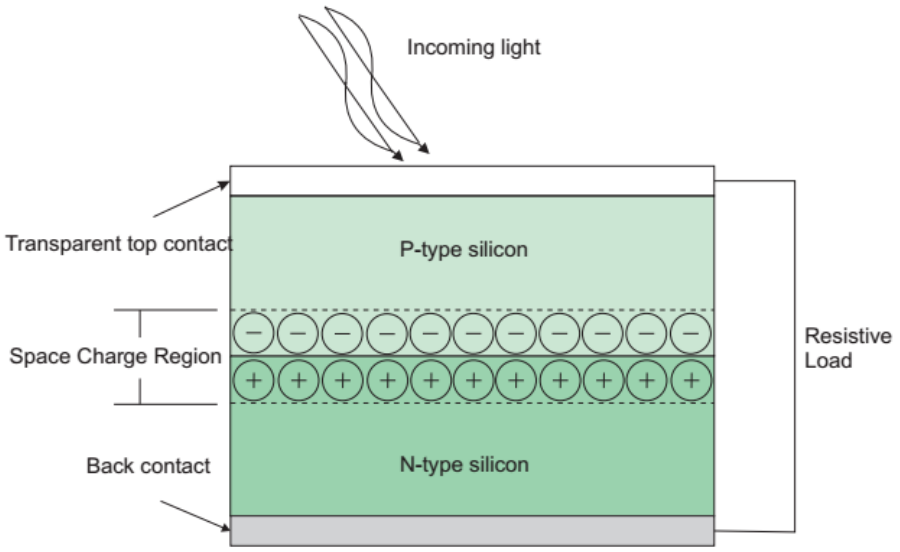

Figure 2: Schematic of operation of first-generation monocrystalline photovoltaic solar cell [2]

The main sources of efficiency loss in all generations of solar cells are:

- Reflection of light from the surface (and back contact for thin film solar cells)
- Absorption losses within the material
- Thermal losses from high energy photons
- Carrier recombination and losses from the contacts

Reflection of light from the top surface of the cell causes losses in the efficiency of the device because a percentage of the incident photons with enough energy to create an electron hole pair in the solar cell are lost. Absorption losses within the material are due to the inability of the material to take advantage of the whole incident solar spectrum. This is due to the singular band gap properties of each material where photons with energy below the band gap do not interact with the material and hence are transmitted through it. Moreover, photons with energy above the band gap, which have more energy than required to create an electron-hole pair, waste their extra energy as heat. Finally, when a photon succeeds in creating an electron-hole pair, the charge carriers have to be efficiently extracted before it recombines in the crystal lattice. [2]

2.2.2 Organic solar cells

Low in cost, light in weight and flexible in mechanics, the solution-processed organic solar cells have aroused worldwide interest and have been the promising alternative to the traditional silicon-based solar cells [3]. However, they are still not available for the commercialization due to their low power conversion efficiency (PCE). Therefore, many research works have focused on the employing of new materials and device structures to improve the device performance. The milestone is the introduction and application of the bulk heterojunction structure consisting of an interpenetrating network of electron donor and acceptor materials [4]. By using this structure, the conventional organic solar cell (OSC) with poly(3-hexylthiophene)/[6,6]-phenyl C61-butyric acid methyl ester (P3HT:PCBM) blend shows a superior performance. Recently, the inverted organic solar cell (IOSC, in which the polarities of the two electrodes are exchanged) has also been introduced as the possible candidate for OSC to remedy the low air stability of OSC [5].

As is well known, the working principle of organic photovoltaic devices can be simply described as a process of 'light in- current out'. This process consists of seven parts:

1. in-coupling of photon,
2. photon absorption,
3. exciton formation,
4. exciton migration,
5. exciton dissociation,
6. charge transport, and
7. charge collection at the electrodes.

The first two parts are the optical mechanisms of the device and the other parts constitute the electrical aspect. The optical aspect plays a significant role because more incident photons and absorbed photons are the baseline for the better device performance. It has been reported that the internal quantum efficiency (IQE) of organic bulk heterojunction solar cells can reach 100% [6]. Thus the external quantum efficiency (EQE) can be approximately described as the product of IQE and the ratio of the number of absorbed photons in active layer to the number of incoming photons. As a result, the optimization of organic solar cells from the optical aspect is seriously

important. This is why we investigate the device performance of organic solar cells mainly from the optical aspect in this work. [3]

2.2.3 Losses in PVs

The maximum possible efficiency of a solar cell can be estimated from a thermodynamic viewpoint, by considering the conversion of heat from the sun, modelled as a black body at a temperature of 6000 K, to the cell at 300 K. This results in an efficiency of 95% (the Carnot efficiency), or, by a more detailed analysis, 93.3% (the Landsberg efficiency). Real solar cells do not approach these theoretical limits due to losses in the conversion process. [7]

2.2.3.1 Intrinsic Losses

The method for converting solar radiation into useful electricity introduces intrinsic losses which result in efficiencies of real devices being much lower than the Carnot or Landsberg thermodynamic efficiencies. Firstly, the introduction of an energy gap into the process means that incident photons with energies less than the band gap cannot excite valence electrons into the conduction band and so this energy is lost. Secondly, the extra energy imparted to an electron by a photon which has energy above the band gap, is lost to the lattice through thermalization, so that the useful energy contributed by each photon is only equal to the band gap. Shockley and Queisser showed that this mismatch between the solar spectrum experienced on Earth, which extends from wavelengths of about 300 nm into the near infra-red (Figure 3), and a single band gap cell, limits the ultimate efficiency of a solar cell with an ideal band gap (of 1.1 eV) to 44% [9]. A third intrinsic loss is the case of radiative recombination, which is the relaxation of an electron back into the valence band, with the excess energy released as a photon. This radiative current subtracts from the current available for useful work. When this is accounted for, together with a consideration of the size of the solar disk as experienced from Earth, the efficiency limit for an ideal solar cell at 1 sun intensity (i.e. no concentration) is calculated to be approximately 31% [8,9].

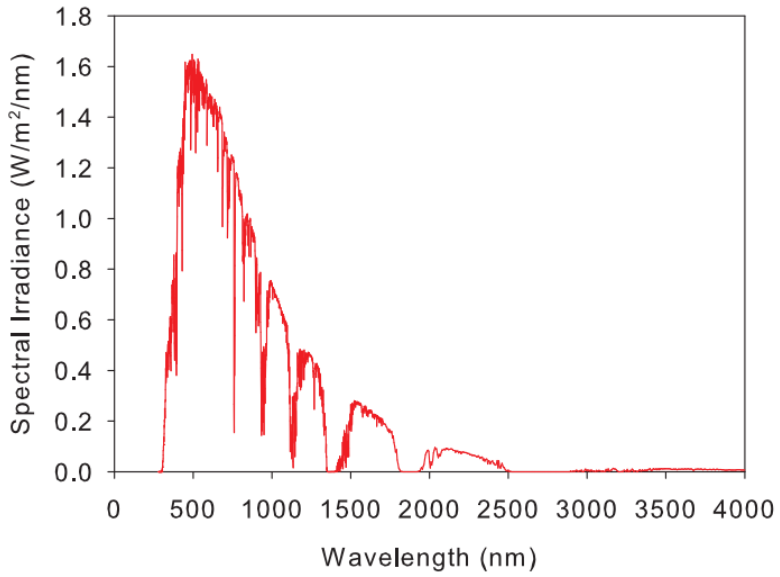

Figure 3: AM 1.5 Reference total solar spectrum (ASTM G173-03), from [11]

2.2.3.2 Optical Losses

In practice, conventional single band gap solar cells suffer from other losses that prevent them even reaching the Shockley-Queisser efficiency limit of 31%. These extrinsic losses fall into two categories: electrical and optical losses. We will focus on the optical losses so the only extrinsic loss that will be mentioned is the recombination at the surface. Carriers that recombine before they are collected do not contribute to the current produced by the cell and so minimizing surface recombination is essential in solar cell design. [8]

Optical losses have a direct effect on the photogenerated current, because they reduce the number of electron-hole pairs created. The three sources of optical loss in a solar cell are:

- Shading by top contacts
- Incomplete absorption of light by material in the cell
- Reflectance from top surface

Research into minimizing shading losses focuses on reducing, or completely eliminating, the surface area covered by top contacts, whilst maintaining a low series resistance. Examples include buried contact cells [10] and interdigitated back contact cells [11]. Incomplete absorption, particularly a problem in thin film silicon cells, can be reduced through light-trapping schemes which involve texturing a surface to force light to travel through more material per pass

and to undergo multiple passes through a cell as a result of total internal reflection [12]. The third optical loss, which is the reflectance from the top surface, is the subject of this thesis. It is already been shown using the Fresnel Equations that, for normal incidence, the reflectance, *R*, from an interface between two materials with refractive indices of n_1 and n_2 respectively is given by

$$R = \left| \frac{n_2 - n_1}{n_2 + n_1} \right|^2 \tag{93}$$

This equation shows that the larger the difference between the refractive indices of the two materials, the greater the reflectance at the interface between them.

The focus of this thesis will be how to minimize the reflectance of solar cell and other materials. Traditional methods of antireflection include the use of destructive interference in the form of thin film coatings and the forcing of light to undergo multiple reflections by texturing on the micron-scale. These are being challenged by new antireflection schemes, inspired by Nature's answer to unwanted reflectance from the eyes and wings of some species of moth. These so called biomimetic "moth-eye" surfaces consist of arrays of pillars with dimensions below that of incident light. They act as a graded index layer which smooths the transition between two adjacent media, reducing reflectance to a very low level. The applicability of such surfaces to solar cells is assessed by analyzing how well reflectance of the useful part of the solar spectrum is reduced. [8]

2.3 Anti-reflection coatings (ARCs)

In this literature review, various methods of achieving antireflection (AR) for solar cells will be explored, from the conventional thin-film antireflection coatings and micron-scale surface texturing to more recent ideas of texturing on a scale below the wavelength of light. Firstly however, the mechanisms by which these AR schemes operate are described.

2.3.1 Anti-reflection mechanisms

2.3.1.1 Destructive interference

In electromagnetic wave theory, when two or more light waves overlap, according to the principle of superposition, the resultant electric field intensity is equal to the vector sum of the

intensities from each wave. Consequently, if two waves are half a cycle out of phase with respect to one another, superposition results in the canceling out of their electric field intensities- the resultant intensity is zero. This is called destructive interference and is the fundamental mechanism behind the common usage of simple thin film coatings to reduce reflection at an interface. Thin film antireflection coatings (ARCs), consisting of one (single-layer ARC), two (double-layer ARC) or more than two (multi-layer ARC) thin film layer(s) of materials with a refractive index in between those of the two media either side of the interface, cause destructive interference between beams reflected from each interface. This results in a minimizing of the intensity in the reflected beams of a particular wavelength for which the coating is designed. [8]

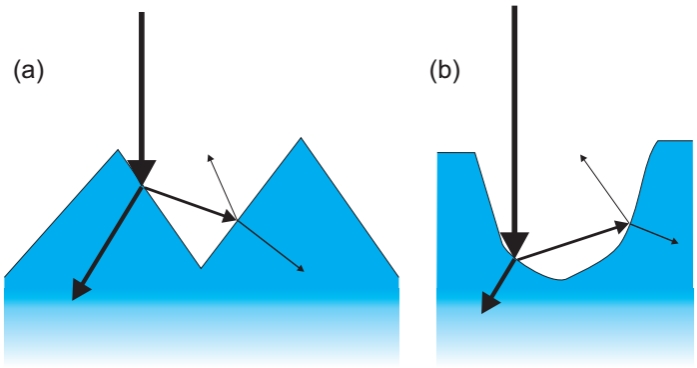

Figure 4: Light reflected from one part of a textured surface is directed to a different part of the surface and so is incident more than once onto the surface of the solar cell, resulting in more light being coupled into the cell: (a) for pyramid-type texturing schemes; (b) for well-type texturing schemes [8].

2.3.1.2 Multiple reflections

Texturing with either regular, geometric features, such as pyramids, or more irregular, random features can lead to a reduction of reflection through a multiple reflection mechanism. One manifestation of this occurs when light reflected from one part of a textured surface is directed onto a different part of the surface and so is incident more than once on the surface of the solar cell, resulting in more light being coupled into the cell (Figure 4). When considering solar cell modules, the presence of a glass cover can lead to another multiple reflection effect: that of total internal reflection (TIR) at the glass-air interfaces as a result of the larger propagation angle of light reflected from a textured surface compared to a planar one (Figure 5).

Light is directed back towards the cell by TIR, resulting in greater transmission of light into the cell. [8]

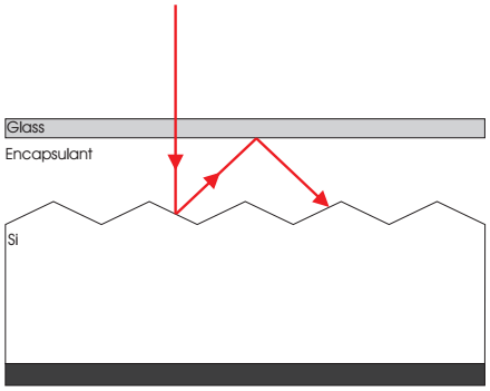

Figure 5: The angle at which the incident light is propagating is changed by reflection from a textured surface such that it now undergoes TIR at the glass interface and is directed back towards the cell [8].

2.3.1.3 Graded refractive index

Removing the step change in refractive index at an interface by texturing it with features on the subwavelength scale can be used to minimize reflection. Most of the solar spectrum lies within the visible range (0.4 - 0.7 μm). When light from the sun interacts with structures of dimensions much below this range, it behaves as if it were encountering a homogeneous medium whose optical properties are a weighted spatial average of the profile's optical properties. If the subwavelength features are regular in size and arrangement, we have what is known as a zero order diffraction grating because all the higher orders are evanescent and only the zero order propagates [13]. Consequently, a surface textured with ridges smaller than the wavelength of light will interact with the light as if it had a single layer ARC of refractive index governed by the ratio between the ridges and channels (Figure 6a). Likewise, a stepped profile will act as a multilayer ARC (Figure 6b) and a tapered profile will behave as an infinite stack of infinitesimally thin layers, introducing a gradual change in refractive index from one medium to the other (Figure 6c). This effectively smooths the transition between one medium and another, ensuring that incident light does not encounter a sudden change in refractive index which would cause a proportion to be reflected. Another way to understand this is to imagine that the subwavelength-structured surface is an infinite stack of infinitesimally thin layers, and so

destructive interference between reflections from each layer cancels out all reflected light, maximizing the proportion of light transmitted. [8]

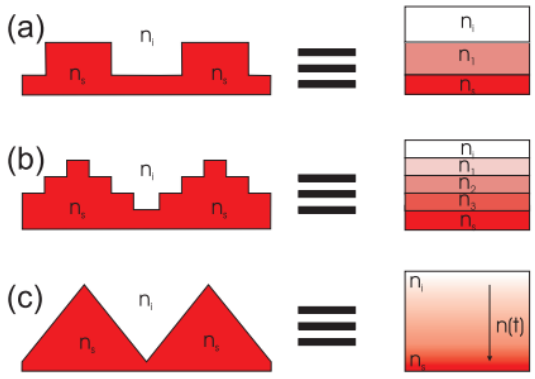

Figure 6: Subwavelength profiles and their analogous refractive index profiles, as experienced by incident light: (a) ridged profile; (b) stepped profile; (c) triangular profile.

2.4 Bioinspired subwavelength anti-reflection structures

The so called “moth-eye” antireflection principle is a type of metamaterial layer that provides anti-reflection by sub-wavelength surface texturing. The textured surface is made up of features that are sub-wavelength in size to that of the wavelength of the incident light. This type of layer is referred to as a “moth-eye” anti-reflection surface in recognition of their discovery on the cornea of a moth’s eye (Figure 7) by Bernhard [14]. The design rules for engineering a ’moth-eye’ surface to a given wavelength spectrum were first outlined in the work of Caplam and Hutley [15].

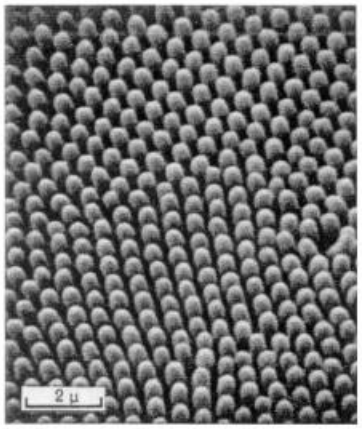

Figure 7: SEM Image of sub-wavelength protuberances on a moth's eye. [14]

Sub-wavelength texturing of materials is a more subtle and biomimetic approach to creating antireflection than long range surface texturing. The principle used is similar to that of anechoic chambers for microwaves and acoustics. Applying texturing on a small enough scale to achieve sub-wavelength antireflection for the visible spectrum is now possible due to the availability of advanced nanoengineering processes like e-beam lithography. The wavelengths of the visible spectrum (400 – 700 nm) are an order larger than the features that can be produced by e-beam lithography (~ 20 nm), a crucial requirement in creating sub-wavelength textures [2].

The ability to texture a material on a scale that is smaller than the wavelength of incident light enables greater control of the optical properties of the interface, by effectively inserting a metamaterial layer between two media. When the features of the structure are smaller than the wavelength of the incident light, they can be perceived as an effective medium which has a refractive index between that of the air and silicon. Depending on the period and size of the feature, a layer with an effective refractive index can be created. The value of the effective refractive index can be any value between that of the two media [17].

'Effective multi-layer' and 'effective gradient index' regions can also be formed by con trolling the shape and profile of the sub-wavelength features. Almost any gradient can be provided by controlling the profile of the features. For instance, a linear gradient can be produced via a conical profile (Figure 8).

One of the main advantages of sub-wavelength texturing is that the ’effective’ refractive index of the interface can be essentially tuned to any intermediate singular value between that of the two media at the interface by changing the spacing period, depth and profile of the nanostructures. Hence the structure of the interface can be chosen in such a way as to optimize the optical response of the layer for any given application [16].

Another crucial advantage of sub-wavelength texturing compared to the other two methods described (thin film layer anti-reflectance and macroscale texturing) is that subwavelength surfaces can work for a broader spectrum and wider angle of incidence.

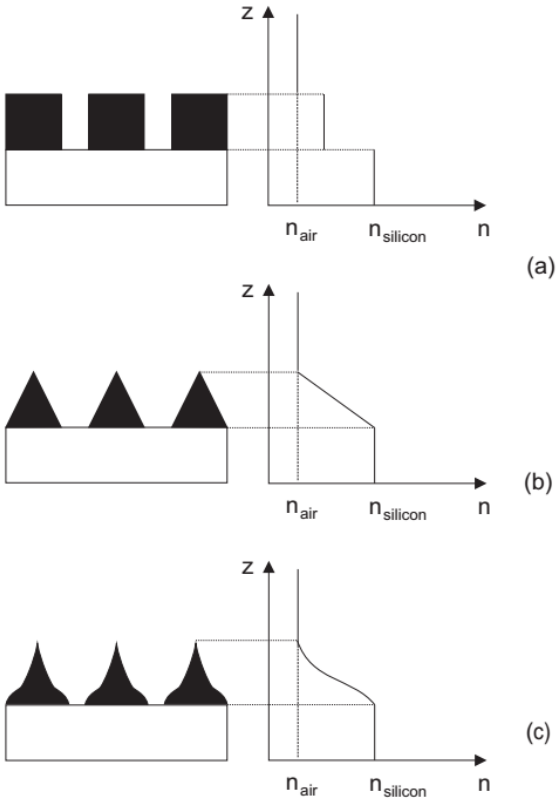

Figure 8: Effect of moth eye shape on refractive index gradient (a) a zero step gradient is equivalent to placing a material with the same thickness and an intermediate refractive index between the two media (b) linear gradient is equivalent to placing a layer with a linearly graded refractive index which starts from the refractive index of air and ends up to the refractive index of silicon (c) a quintic gradient has a similar effect to (b) with the exception that the refractive index gradient is not linear between the two media. [2]

Studies on creating an optimum refractive index gradient and the corresponding surface relief feature profile required to produce a broadband 'moth-eye' antireflection layer have been carried out by Southwell [18]. It was shown that a near-optimum antireflective performance can be achieved in the visible spectrum between two dielectric media when the refractive index varies according to a quintic polynomial as depth is increased [18].

The quintic equation makes the refractive index and its second derivative continuous [18]. The quintic change in refractive index through the layer is defined by equation 94. It has shown to improve performance of the antireflection layer compared to a linear graded index (Equation 95).

$$n_{eq} = n_i + (n_s - n_i)(10t^3 - 15t^4 + 6t^5) \tag{94}$$

$$n_{eq} = n_i + (n_s - n_i)t \tag{95}$$

where n_{eq} is the effective refractive index, t is the depth of the antireflection layer, n_i the refractive index in air, ns the refractive index in substrate.

Texturing a large surface, such as a whole silicon wafer, with nanoscale sub-wavelength features via e-beam lithography is tremendously time consuming and expensive. However, there are some new scalable technologies which are based on e-beam technology such as nanoimprinting which are promising and have the capability of accelerating the texturing process and bringing down the cost but these also have limitations which will be discussed in following chapters.

2.5 Simulation methods

2.5.1 Overview of optical modeling methods

There are many different mathematical models for treating the behavior of electromagnetic radiation through subwavelength anti-reflective structures. These methods include a numerical time-based approach called the finite-difference time-domain (FDTD) method, numerical frequency-based methods of the transfer matrix method (TMM, models thin films only), rigorous coupled wave analysis (also called Fourier modal method RCWA/FMM), coordinate transfer method (C-method), and finite element method (FEM), as well as exact approaches such as Knop's or Sheng's handling of 2D square grooves [19] and geometric optics (ray tracing, which is not appropriate for sub-wavelength structures). Effective media theory

(EMT) is used in conjunction with TMM to assign an effective index of refraction to discretized layers of an interface that make up subwavelength structures or other gradient index (GRIN) materials [19]. Each of these methods has its benefits and limitations in modeling the behavior of light through ARCs and those that have been used in this thesis will be discussed in the following sections.

2.5.2 Transfer Matrix Method (TMM)

The transfer matrix method (TMM) is a simple approach to modeling waves passing through layered media. Appropriate only for thin film ARC modeling, this method employs continuity boundary conditions between layers of material and wave equations to describe the electric fields or reflectance and transmittance values across each layer. Continuity requires that the fields at the interface between two materials be the same in each material. Then, if the electric field is known at the beginning of the layer a transfer matrix based on the wave equation can be used to determine the electric field at the other end of the layer (see Section 2.1.2). Both reflected and transmitted waves are considered to calculate the overall electric fields [19].

2.5.3 Finite Difference Time Domain (FDTD) method

The finite-difference time-domain (FDTD) numerical modeling method is considered to be one of the most accurate and simple rigorous methods to model anti-reflective properties of sub-wavelength structures. Though it is computationally intensive, the FDTD method handles any arbitrarily shaped structure naturally using an explicit numerical solution to Maxwell's curl equations. The FDTD method was first introduced in 1966 by Yee and was furthered by Taflove [20,21]. Yee developed the mathematical approach to spatially discretize the computational space into what is now known as a Yee cube (Figure 9). The Yee cube is the unit cell of the equally offset electric and magnetic field computation points.

The Yee FDTD algorithm can be summarized as [29,30]:

- Replace all the derivatives in Ampere's and Faraday's laws with finite differences. Discretize space and time so that the electric and magnetic fields are staggered in both space and time.
- Solve the resulting difference equations to obtain "update equations" that express the (unknown) future fields in terms of (known) past fields.
- Initialize the fields to some known state (usually zero).

- Introduce energy to the computational domain via a suitable method.
- Evaluate the magnetic fields one time-step into the future so they are now known (effectively they become past fields).
- Evaluate the electric fields one time-step into the future so they are now known (effectively they become past fields).
- Repeat the previous three steps until the fields have been obtained over the desired duration.

Thus, the basic idea of the FDTD algorithm is that the time-dependent Maxwell's curl equations are discretized using central-difference approximations to the space and time partial derivatives. The resulting finite-difference equations are computed in a leapfrog manner so that the electric field vector components in space are solved at a given instant in time and the magnetic field vector components are solved at the next instant in time. The process is repeated over and over again until the field has achieved a desired state (e.g., gone to zero).

The FDTD method, described thoroughly in Taflove's book 'Computational Electrodynamics: the finite-difference time-domain method' [22] was first developed to model electromagnetic (EM) radio waves. However, due to the simple and versatile approach, it is able to naturally handle any EM modeling situation given sufficient computing resources [19].

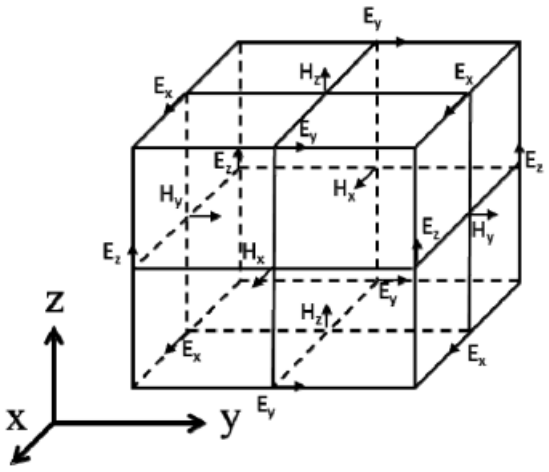

Figure 9: Yee cell. Arrows indicate the direction of the E or H field that is calculated at each point [19].

2.5.4 Effective Medium Theory (EMT) method

Unlike the other modeling methods reviewed in this paper, effective medium theory (EMT) is not a method for directly determining reflectance or transmittance of an ARSWS. Instead, this is a method that determines the effective index of refraction of a sub-wavelength structured geometry based on the volume fill factors of the multiple materials (Figure 10). As shown here, EMT is only valid when the period of the texture is much smaller than the wavelength of light; some authors consider EMT only valid when the period is less than one tenth the wavelength [23]. At larger feature sizes EM waves behave in the Bragg regime, where only one or two diffraction orders are present in the diffracted (reflected or transmitted) light. Larger feature sizes require modeling of higher order diffractions and cannot considered gradient index (GRIN) materials or effective media [19].

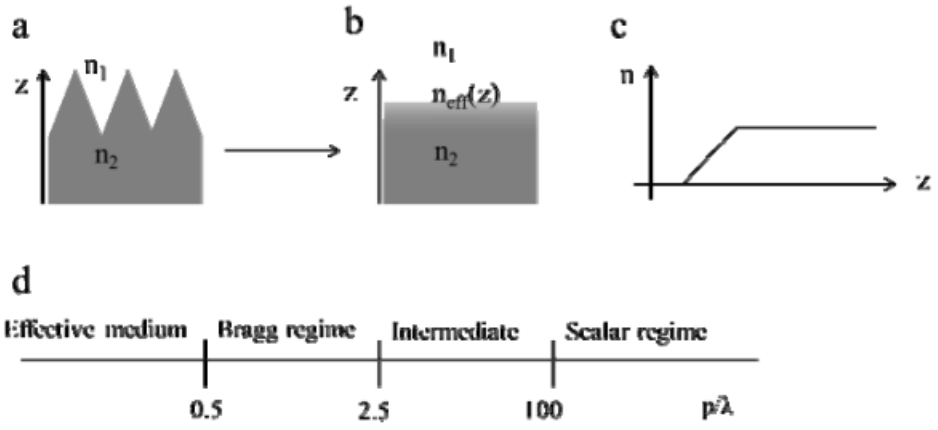

Figure 10: Schematic of a graded index subwavelength structure (a); the effective index of refraction according to how the light would interact with the material (b); and a graph of an approximate effective index (c); The various regimes of optical behavior with grating sizes are shown in (d), indicating that the effective medium theories are applicable for gratings whose periods (p) are much smaller than the wavelength of light (λ) [19].

2.6 Fabrication techniques for sub-wavelength nanostructures

2.6.1 Photolithography

Photolithography defines patterns by forcing light to sensitize a photo resist in specific areas via a mask that defines dark and bright regions on the resist. There are several ways of setting up this mask layer in relationship with the substrate: contact lithography, where the mask is in contact with the substrate; proximity lithography, where the mask and resist are very close

to each other; and projection lithography where an optical system exists between the mask and resist.

There are two types of mask that can be used, conventional 'shadow' generating masks and phase-change masks. A phase-change mask is able to take advantage of destructive interference of the diffracted light by inducing a phase change of half the wavelength in the light shown through one of the slits so that a smaller spacing between features is possible. The main disadvantage of phase change masks is that they are expensive to make.

There are two kinds of photo resist available which are useful in different pattern design scenarios. One is called a positive and the other is called a negative resist. A positive resist becomes soluble when activated by the light exposure process, whereas the negative resist hardens when exposed to light. The choice between resists depends on the design required. For example, in a serial process like e-beam lithography, if the design is such that the majority of the resist needs to be removed from the wafer, then in order to minimize write time, the beam will be exposed to the parts which need to remain on the wafer as they consume less space and thus will take less time to write, so a negative resist would be used. In the opposite case a positive resist would be used. In either case, the definition of the mask would be optimized for minimum write time. In photolithography this is less of an issue because the light floods the whole wafer, but a mask still needs to be designed and if the write time for the mask needs to be minimized it will influence the decision of which resist to use in a similar fashion.

Photolithography is very fast at accomplishing large area patterning because it is a 'parallel' technique. Light is illuminated on the whole mask to form the projection of the required image on the resist for the small amount of time required to harden the resist. It is hence fast enough to be used for mass production. Historically, a relatively simple alteration used to reduce the size of the features created by photolithography is decreasing the wavelength of light used in the process. Wavelength is one of the factors that limits the size of features which can be created via photolithography as described by the Rayleigh formula (Equation 96) along with the Numerical Aperture of the lens and the process factor.

$$\Delta x = k_1 \lambda / NA \tag{96}$$

where k_1 is a process factor determined by the exact details of the optical system, λ is the wavelength and NA the numerical aperture [2].

By reducing the wavelength used in the photolithographic process, the microelectronics industry has been able to keep up with the continuous need of reducing the size of transistors built for processing chips in order to make them faster. In particular, Moore's law of exponentially scaling down the size of the transistors will be available until the physical limits of the technology come into play. Moore's law is the infamous empirical observation made by Intel co-founder Gordon E. Moore, that the number of transistors which can fit in a silicon die are doubled every 18 months. This observation has since become a fundamental guideline which the microprocessor industry uses for designing new product cycles.

Photolithography has pushed the boundaries of the length of the minimum features it can inscribe from 365nm in 1996, to 45nm in 2009 by using Deep Ultra Violet Photolithography (DUV) (λ = 139nm). With an expected jump to Extreme Ultra Violet Lithography (λ = 13nm) (EUV) it seems that lithography has some lifetime yet before becoming completely obsolete and is currently successfully being preferred to other nanoengineering methods. However, the smaller the wavelength, the lower the tolerances for error in designing the optics of the system (lenses etc.) and the harder the mask creation [2,24]. Additionally there is no optical system known to manipulate wavelengths that are smaller than Deep UV part of the spectrum (i.e. for X-Rays and Gamma rays).

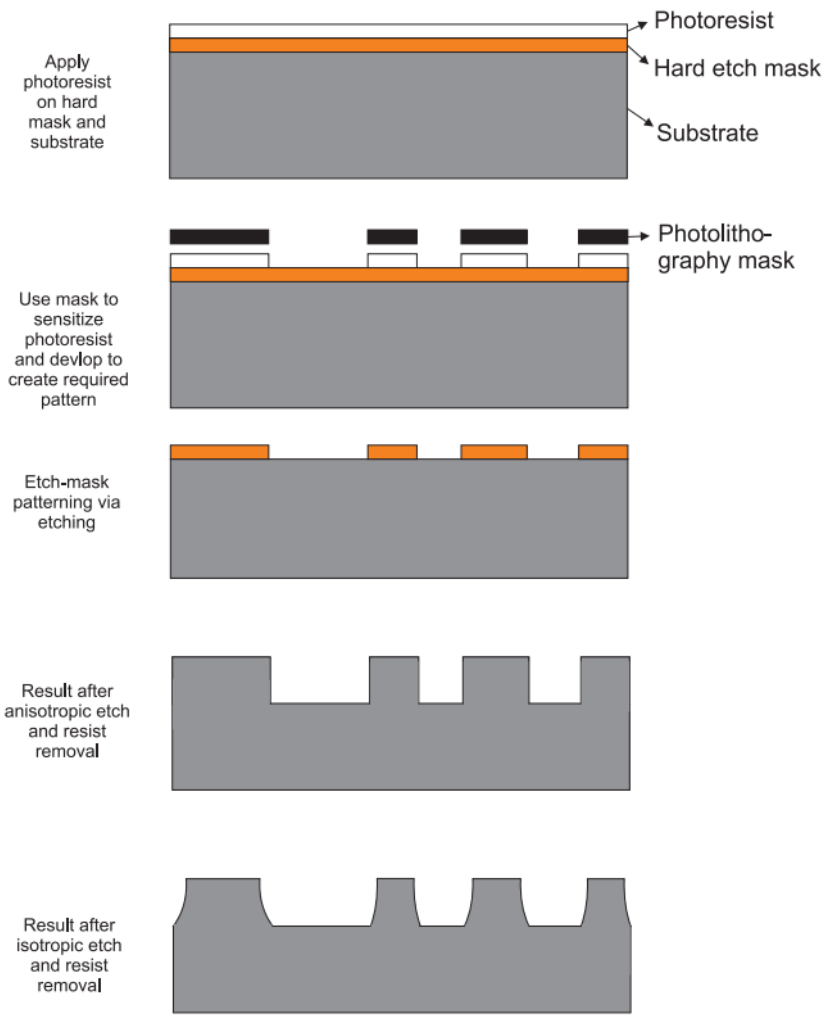

Figure 11: Process steps in creating pattern via photolithography [2].

Reducing the wavelength of the photolithography process has worked so well this far because the transition costs of 'improved' versions of this technology relatively 'low' because only the light source and the optics of the system need to change, not the whole installation. The disadvantages of using photolithography for nanoengineering are that nano-scale feature sizes are not readily available yet (i.e. smaller than 45nm) and X-Ray, EUV technologies are still under development. It is also very difficult to create optical projection systems with wavelengths in the EUV and X-ray spectra [2,25].

2.6.2 Electron-beam lithography

In e-beam (or electron-beam) lithography, a beam of electrons is used to sensitize a resist. A typical e-beam process is shown in Figure 12. The electron dose of the beam needs to be optimized for each resist material and thickness. A commonly used resist is PMMA (poly methyl methacrylate).

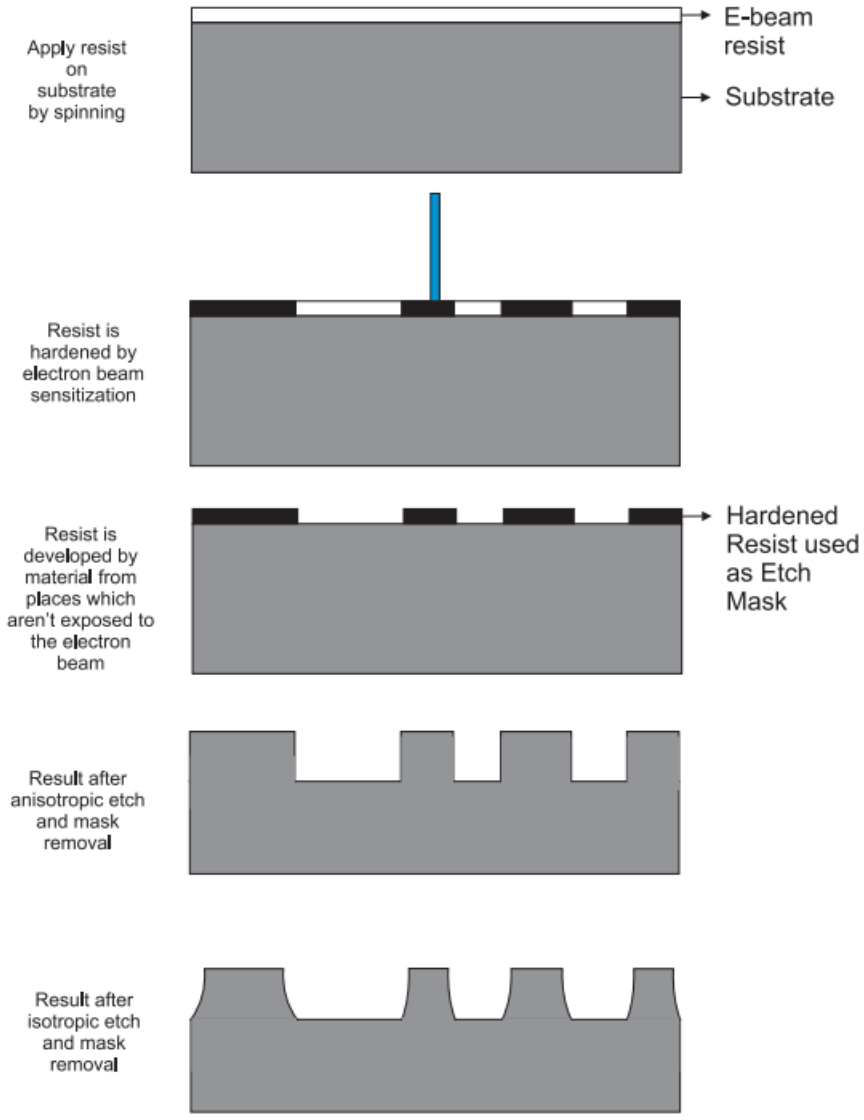

Figure 12: Process steps in creating pattern via e-beam lithography [2].

The operation of the e-beam machine is similar to an SEM (Scanning Electron Micro scope) where an electron beam is created and focused onto the sample. However instead of using electrons to image the sample, the electron beam sensitizes the negative resist in specific areas to

make the pattern. The beam is moved around by applying an electric or magnetic field and a total pattern size of 100 by 100μm can be written at once. For large patterns, it is possible of stitching the image if the stage is able to provide very accurate movement of the substrate. The limits of e-beam technology are related to the electron scattering within the resist, this is known as the proximity effect. The proximity effect describes the high probability of the injected electron traveling laterally in the resist and sensitizing a much larger resist area than the diameter of the beam. The limit of fundamental feature size which can be resolved depends on the magnitude of this effect. This is why feature sizes are limited to 10-20nm in most cases, even though the size of the electron beam is much smaller.

The greatest advantage of e-beam lithography is that it can produce very small feature sizes of any type of pattern across the substrate because the location of the beam on the sample can be controlled very precisely via a computer file created from a CAD program. Additionally, there is no mask needed so there are no limitations associated with the mask (such as diffraction and optics, which are additional limitations in photolithography) because the exposure is defined by aiming the electron beam at the areas which are necessary and switching the beam on and off to control the electron dose.

The main limitation in applying e-beam lithography to industrial processes is that it is a ’serial’ process where each feature is defined individually. Hence, it takes much more time to define a large pattern compared to ’parallel’ techniques such as photolithography were a whole wafer is defined at once. This slow process is a major factor which leads to very high manufacturing costs, rendering the method impractical for commercialization [26]. However, it does produce very good results and is very useful in prototyping [2].

2.6.3 Nano-imprint lithography

In Nano-Imprint Lithography (NIL) there are two basic methods of defining patterns. Their difference resides in the method used to mold the soluble resist. One method uses thermal energy to harden the material and the other uses UV radiation for the same purpose. Before the NIL process begins, a master is designed and patterned by e-beam lithography; this master is then used to transfer the pattern onto the substrate. The soft resist material that is to be patterned is placed on the top surface of the substrate in liquid form. The master is then brought into contact with the material that is molded via pressure and heat to make the material form and

harden. The master is removed and the excess material is then etched away from the substrate. The final etch mask pattern is thus created. The substrate material is ready to be etched so that the resist pattern is transferred to the substrate. The main advantage of using this technology compared to e-beam lithography is that essentially it can create reproducible patterns on a very large substrate in a parallel manner, which is much faster than using e-beam lithography alone. It also allows for an alternative technology to e-beam that is suitable for mass production. Very small minimum features have been achieved using this technique (~ 14nm) [27]. The main disadvantage of using NIL is that the initial stamps are created by an e-beam process which makes prototyping very time consuming [2].

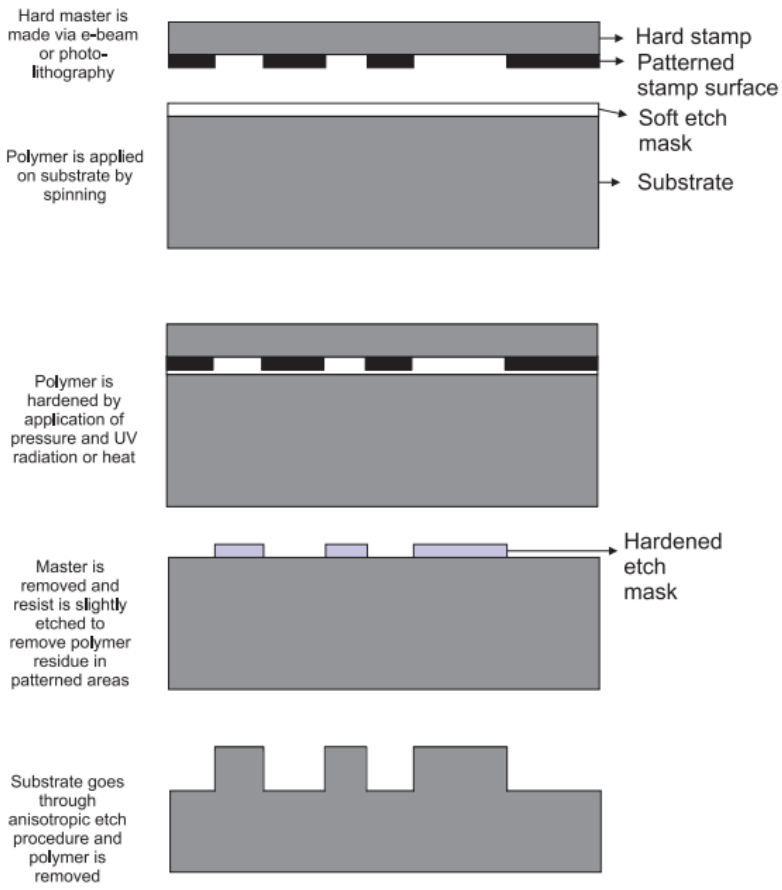

Figure 13: Process steps in creating pattern via nano-imprint lithography [2].

Hubbard et al [28] have recently demonstrated a wafer-scale nano-imprinting method that uses disposable masters to reduce the cost and increase the speed of nano-imprint lithography. This allows for kilometers of disposable masters to be created very cheaply. The pattern is then

applied onto the resist by bringing it into contact with the disposable master and applying minimal pressure. The final pattern is transferred to the substrate via dry etching [2].

3 Chapter 3 – Simulations of thin film ARCs

3.1 Overview

The literature review revealed that thin film coatings (ARCs) are commonly used to achieve antireflection in solar cells (Chapter 2). Materials are chosen with appropriate optical properties and deposited to thicknesses which lead to destructive interference between light reflected from the interfaces in the thin film structure. Destructive interference reduces the amount of reflected light and so increases the amount transmitted into the underlying cell. The amount of destructive interference and therefore the reflectance and transmittance of a substrate coated with a thin film ARC is heavily dependent on the wavelength and incident angle of incoming light.

3.2 Transfer Matrix Method (TMM)

There are various methods of calculating the reflectance and transmittance of a thin film coating and these are detailed in many optics textbooks [8]. In this work, the transfer matrix method is employed to determine the reflectance by using. Maxima is a system for the manipulation of symbolic and numerical expressions, including differentiation, integration, Taylor series, Laplace transforms, ordinary differential equations, systems of linear equations, polynomials, sets, lists, vectors, matrices and tensors. Maxima yields high precision numerical results, by using exact fractions, arbitrary-precision integers and variable-precision floating-point numbers. Also Maxima can plot functions and data in two and three dimensions [33].

In Maxima a powerful script was developed from scratch. This script has the capability to calculate and plot reflectivity (and/or transmissivity) for any case of layered thin-film structure accepting as inputs the refractive index of the medium that the light is initially propagating (i.e. air), the refractive index and thickness for each layer that consists a particular system and the refractive index of the substrate.

3.3 Single-layer anti-reflective coatings (SLARCs)

The first thin-film coating simulation involves a single-layer coating with an ideal refractive index on a glass substrate with refractive index $n_g = 1.5$. The refractive index of the anti-reflection layer is calculated using Equation 87 and is equal to $n_l = \sqrt{1.5}$. It is a quarter-wavelength coating which means that its thickness is $d = \lambda_t/4$, where λ_t is the target wavelength where reflectivity equals zero. In Figure 14, the reflectivity across a wide range of wavelength (300 nm – 1200 nm) is represented, and in this ideal situation, the reflectivity equals zero at the target wavelength (550 nm).

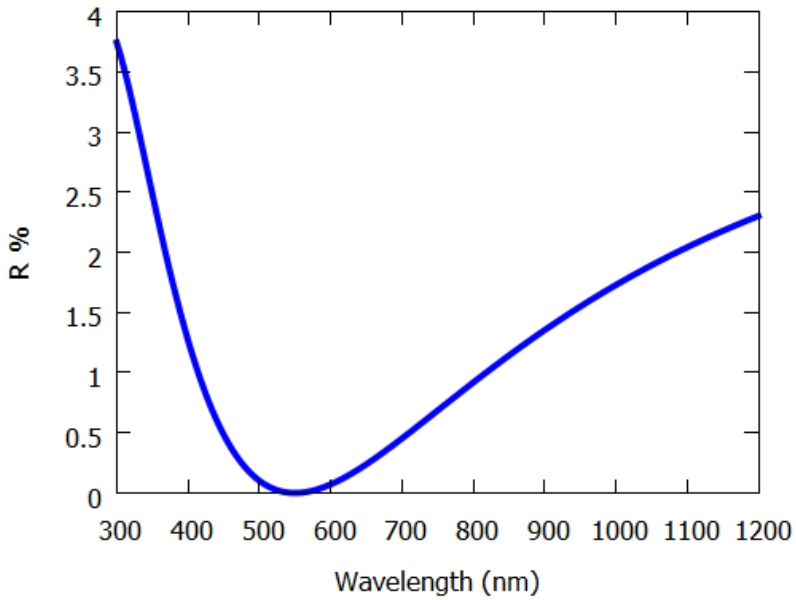

Figure 14: Optimum single-layer anti-reflection coating (ARC)

The second case is that of the most commonly used single-layer anti-reflection coating, which is the magnesium fluoride MgF_2 with refractive index $n = 1.38$. The simulation parameters remain the same, namely, a glass substrate with refractive index $n_g = 1.5$ and thickness $d = \lambda_t/4$. In Figure 15, the reflectivity across a wide range of wavelength (300 – 1200 nm) is represented, and the reflectivity has a minimum of ~1.4% at the target wavelength (550 nm). Also, it is observed that in the visible region (400 – 700 nm), the reflectivity remains below 2%.

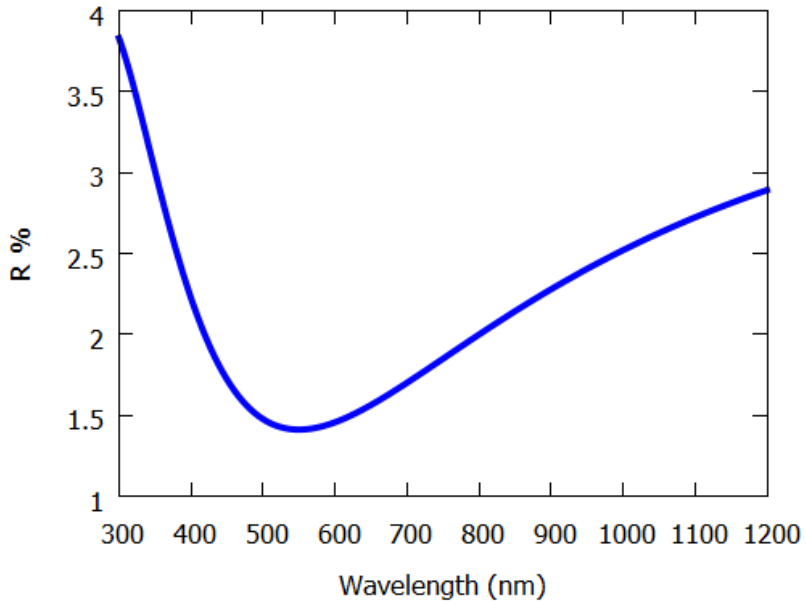

Figure 15: Common MgF_2 single-layer anti-reflection coating (ARC)

3.4 Double-layer anti-reflective coatings (DLARCs)

Double layer antireflection coatings (DLARCs) can be designed to provide a broader band AR effect than SLARCs. With two layers, more parameters are available for optimization and destructive interference is optimized for more than one central wavelength.

At first, the case of *double-quarter, single-minimum* is considered [1]. This case describes a double-layer anti-reflection coating where each is a quarter-wavelength coating, with thicknesses $d_1 = \lambda_t/4$ and $d_2 = \lambda_t/4$, which results in a single minimum in the reflection spectrum as shown in Figure 16. The simulation parameters involve a glass substrate with refractive index $n_g = 1.5$, while the first layer (top) is magnesium fluoride MgF_2 with refractive index $n_1 = 1.38$ and bottom layer is cerium trifluoride CeF_3 with refractive index $n_2 = 1.63$. These coatings are the perfect solution especially for laser applications, where resistance to intensive laser radiation is important and minimum reflection is required only at a specific wavelength [47].

In Figure 17 though, the reflectivity across a wide range of wavelength (300 – 1200 nm) is represented for the same simulation parameters, but in this case, the thickness of the second

layer, the cerium trifluoride CeF_3, is $d_2 = \lambda_t/2$. This design results in reflectivity with two minima and one weak central maximum and broader anti-reflection range.

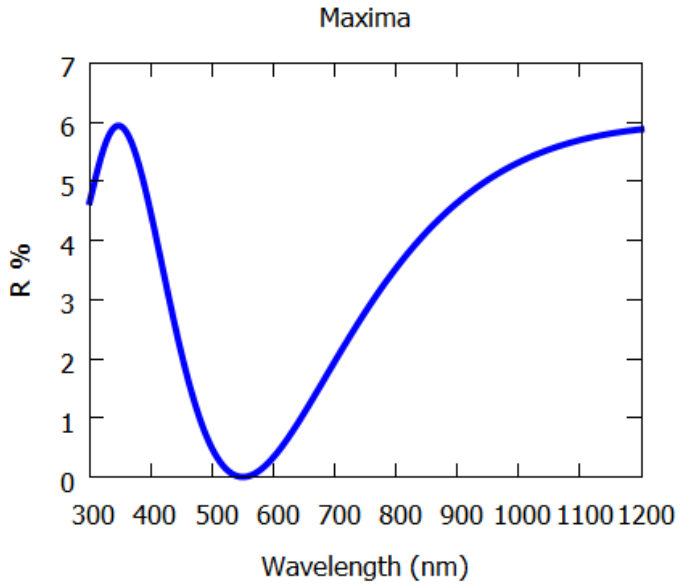

Figure 16: Double-quarter single-minimum double-layer anti-reflection coating (ARC)

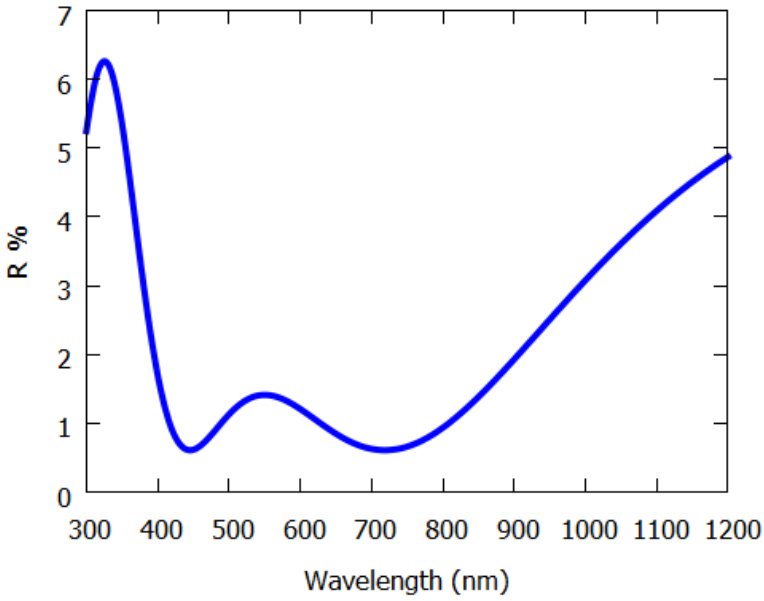

Figure 17: Double-layer anti-reflection coating (ARC) tuned to two different minimum wavelengths

3.5 Multi-layer anti-reflective coatings (MLARCs)

Having already discussed what happens in the case, firstly, of single-layer anti-reflection coatings and then the double-layer anti-reflection coatings, it is time to add one more layer in the anti-reflection scheme. Now, the simulation concerns Edmund Optics triple-layer anti-reflection coating design, where the layers that compose this design are magnesium fluoride MgF_2 with refractive index $n_1 = 1.38$ as the first layer, tantalum pentoxide (Ta_2O_5) with refractive index $n_2 = 2.15$ as the second layer and aluminum oxide (Al_2O_3) with refractive index $n_3 = 1.70$ as the third layer. Once more, the substrate is glass with refractive index $n_g = 1.5$. Figure 18 visualizes the structure of this design regarding the materials and their respective thicknesses. QWOT stands for quarter-wave optical thickness $d = \lambda_t/4$, while HWOT stands for half-wave optical thickness $d = \lambda_t/2$. In Figure 19, the reflectivity across a wide range of wavelength (300 – 1200 nm) is represented, where in the visible region (450 – 700 nm), the reflectivity remains below 0.5%.

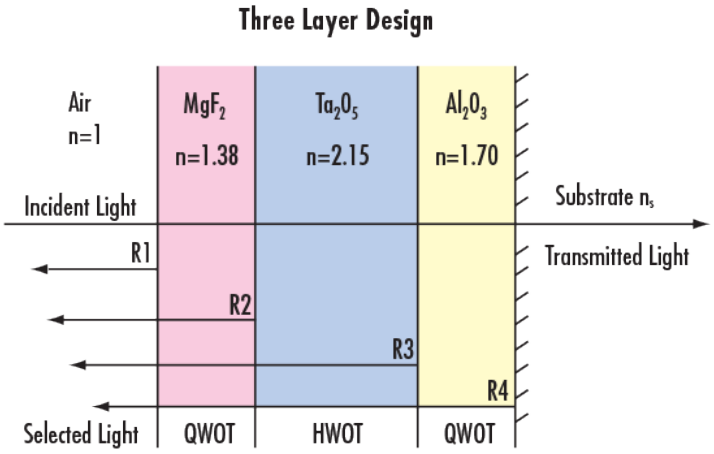

Figure 18: Edmund Optics triple-layer anti-reflection coating design

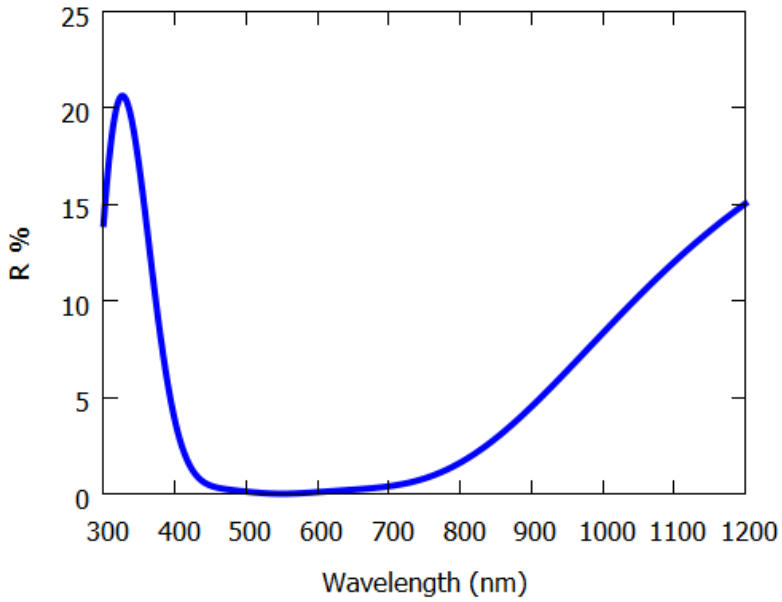

Figure 19: Triple-layer anti-reflection coating (ARC)

3.6 Multi-layer periodic systems

The simplest kind of periodic system is the *quarter-wave* stack, which is made up of a number of quarter-wave layers. The periodic structure of alternately high- and low-index materials is illustrated in Figure 20. This case is studied in order to show that with the script developed in Maxima it is possible, not only to simulate thin-film anti-reflection coatings but also, reflective structure such as Bragg reflectors or Fabry-Perot filters.

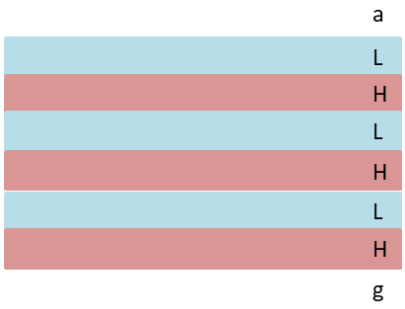

Figure 20: Reflective periodic structure

Figure 21 illustrates the general form of a portion of the spectral reflectance for a few quarter-wave $(d = \lambda_t/4)$ multilayer filters. For the simulation, magnesium fluoride MgF_2 with

refractive index $n_L = 1.38$ serves the low-index layer (L), while zirconium dioxide ZrO_2 with refractive index $n_H = 2.1$ serves the high-index layer (H). It is clear that the height of the high-reflectance central zone increases with the number of layers added. Note that the maximum reflectance of a periodic structure such as $g(HL)^m a$ can be increased further by adding another H-layer, so that it has the form $g(HL)^m Ha$.

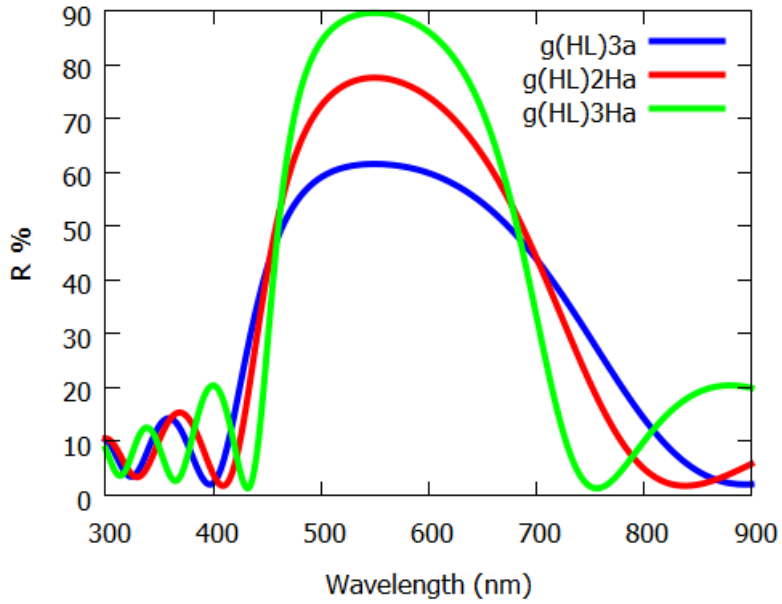

Figure 21: Reflective multi-layer periodic stack (Bragg reflector)

4 Chapter 4 – Simulations of moth-eye AR structures

4.1 Overview

The concept of reducing reflection by texturing a surface with features on the subwavelength scale was introduced in the literature review (Chapter 2). We learned that incident light cannot resolve the individual features on a subwavelength-textured surface and so the patterns exhibit an effective refractive index dependent on the ratio of the substrate material to air. The shape of the features causes this ratio to gradually increase from air into the substrate, leading to a gradual increase in effective refractive index. This eliminates the discontinuity in refractive index at the interface and so minimizes reflection. Studies show that these surfaces exhibit low reflectivity over broad ranges of wavelength and angle of incidence [8] and so could be more effective than thin film ARCs for reducing reflection over a day. We also discovered that subwavelength patterning is used for AR in nature, specifically on the eyes and wings of

some species of moth. These ‘moth-eye’ surfaces have evolved to reduce reflection of sunlight, which makes them particularly applicable to solar cells.

4.2 Finite-Difference Time-Domain (FDTD) simulations

The simulation program FDTD solutions by Lumerical solutions Inc., can be used to accurately simulate sub-wavelength photonic and optical devices and can be used in many applications such as integrated optics, nanoparticles scattering, plasmonics, solar cells and many more. Lumerical allows design and optimization in 2D and 3D TCAD context and add sources and monitors to simulation. It has the ability to run parallel simulations in any available computer resource to obtain normalized transmission or reflection simulations, diffracted order from gratings and other periodic structures and many other features, the results can be readily analyzed. Lumerical can run parameter sweeps and has a conformal mesh FDTD simulator which makes simulation runs faster and allows more accurate results than a stair case mesh.

In the design each material is allocated a different color (Figure 20). The FDTD object is the simulation region. The boundary conditions for an object can make simulations simpler by selecting periodic or symmetrical boundaries. For the majority of simulations used in this study, periodic boundaries have been used for the vertical sides of the simulation region, and Perfectly Matched Layer (PML) boundaries for the horizontal sides of the simulation region.

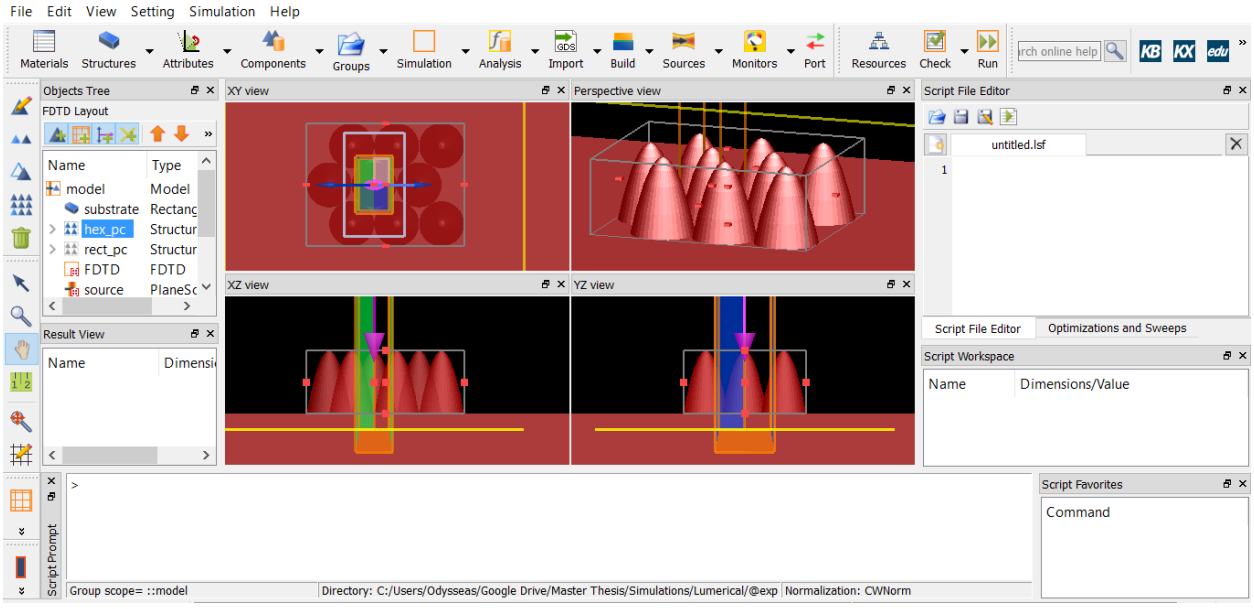

Figure 22: Lumerical FDTD Solutions simulation window

The source object simulates the incident light, for all of the simulations in this study; a plane wave source with wavelengths in the range 300-1000 nm was used in order to simulate a solar source. Monitors collect data and are represented in the Lumerical display by yellow boxes or lines. Two different types of monitor have been used in these simulations; movie monitors create an animation of the simulation. Frequency domain power monitors measure several properties, including transmission T and electric field E.

4.3 Simulation setup

4.3.1 Refractive index data

4.3.1.1 Silicon

Optical data for n and k for silicon over a range of wavelengths is obtained from [34].

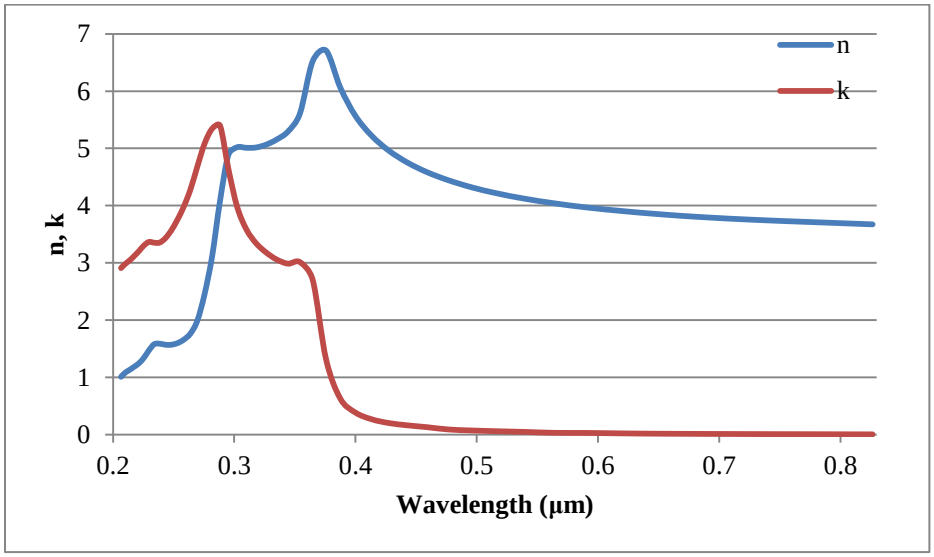

Figure 23: Silicon optical constants [34].

4.3.1.2 PMMA

Optical data for PMMA over a range of wavelengths is obtained from [35]. The function which describes the refractive index dispersion is

$$n^2(\lambda) = a_0 + a_1\lambda^2 + a_2\lambda^4 + a_3\lambda^{-2} + a_4\lambda^{-4} + a_5\lambda^{-6} + a_6\lambda^{-8} \quad (97)$$

with the parameters a_0- a_6 defined in Table 1.

Table 1: Refractive index fit coefficients

a_0	2.1778e+0
a_1	6.1209e-3
a_2	-1.5004e-3
a_3	2.3678e-2
a_4	-4.2137e-3
a_5	7.3417e-4
a_6	-4.5042e-5

In Figure 24, the refractive index dispersion as a function of wavelength is represented

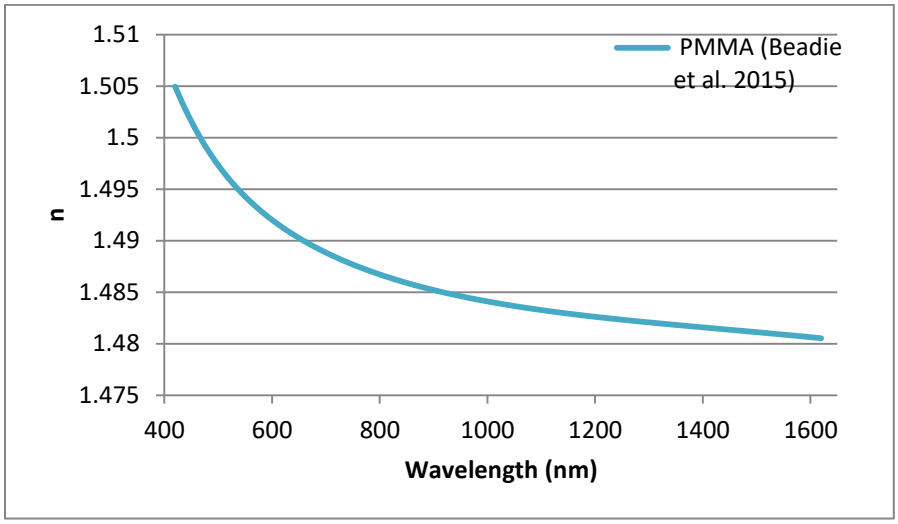

Figure 24: PMMA optical constants [35].

4.3.1.3 PEDOT:PSS

Optical data for the real and the imaginary part of the refractive index of PEDOT:PSS, which constitutes the transparent electrode in the organic solar cell reflectivity simulations, over a range of wavelengths is obtained from [36,37].

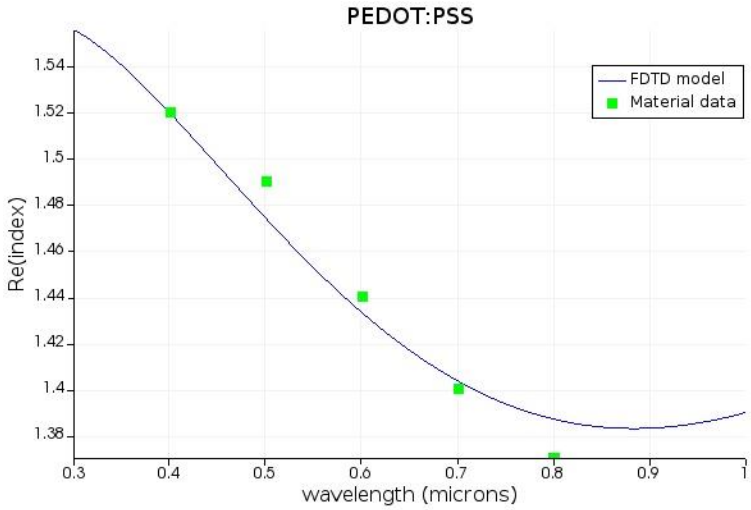

Figure 25: Refractive index real part of PEDOT:PSS [36,37].

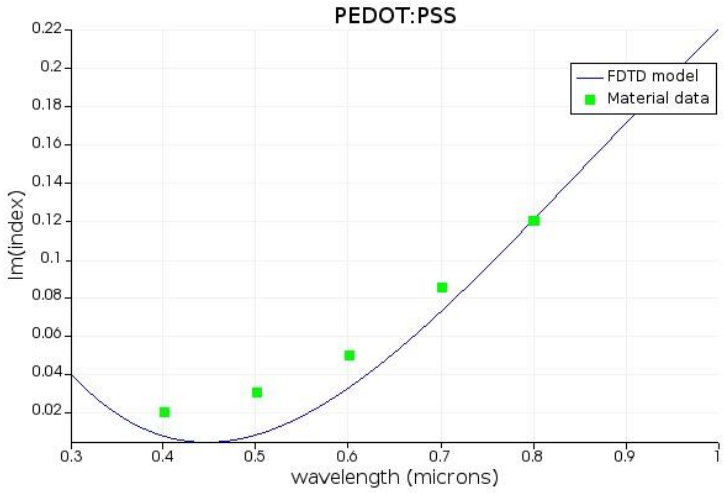

Figure 26: Refractive index imaginary part of PEDOT:PSS [36,37].

4.3.1.4 P3HT:PCBM

Optical data for the real and the imaginary part of the refractive index of P3HT:PCBM, which constitutes the active layer in the organic solar cell reflectivity simulations, over a range of wavelengths is obtained from [36].

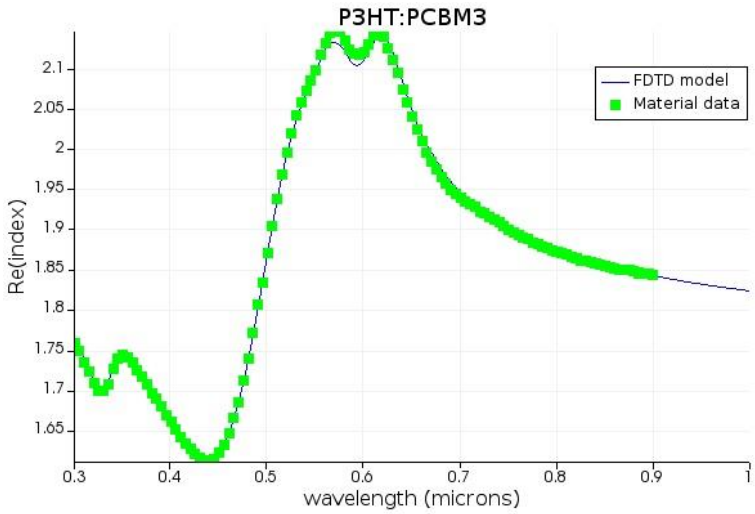

Figure 27: Refractive index real part of P3HT:PCBM [36].

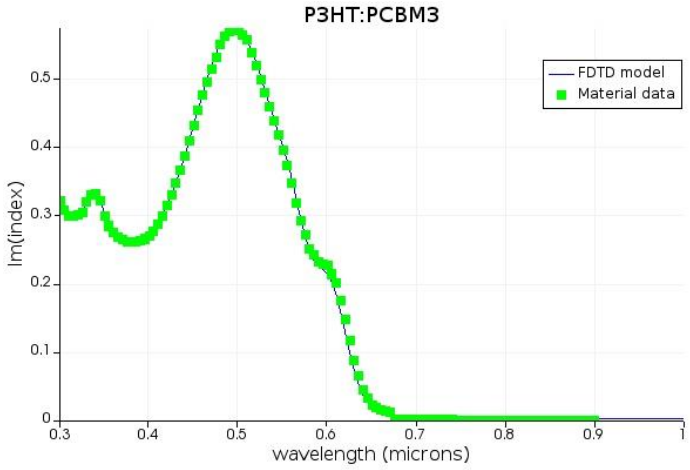

Figure 28: Refractive index imaginary part of P3HT:PCBM [36].

4.3.1.5 Ag (silver)

Optical data for the real and the imaginary part of the refractive index of Ag, which constitutes the metal electrode in the organic solar cell reflectivity simulations, over a range of wavelengths, is obtained from [38].

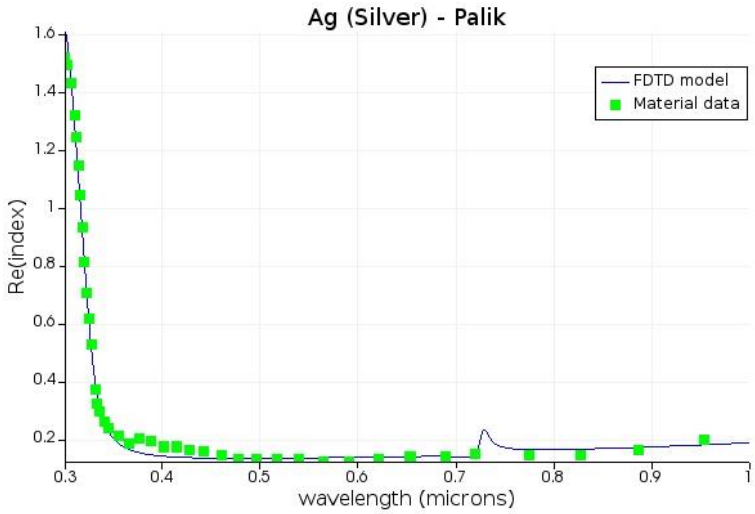

Figure 29: Refractive index real part of Ag [38].

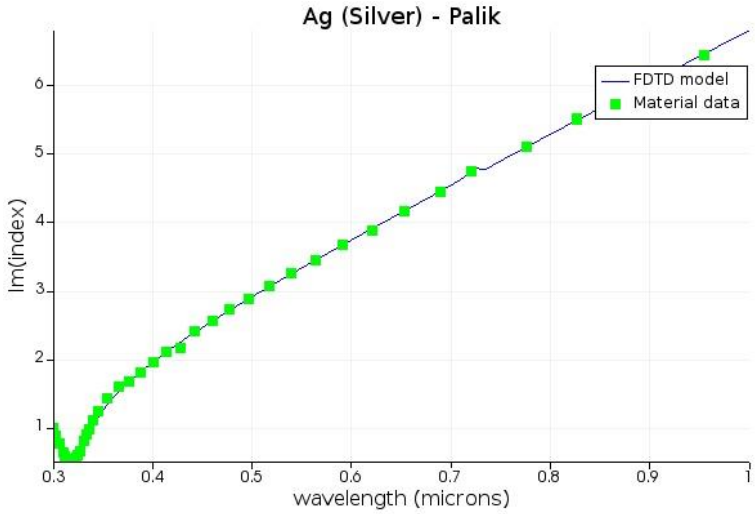

Figure 30: Refractive index imaginary part of Ag [38].

4.4 Bibliography experimental results validation

In order to ensure that the finite-difference time-domain (FDTD) software that was used, is properly configured and the simulation results are correct, an extensive comparison of the results with these of bibliography has been made, for various types of cases. Data used for comparing graphs, obtained by digitizing graphs from the literature using Web Plot Digitizer, an HTML5 based tool to extract numerical data from plot images. The first two cases, concerns thin-film anti-reflection coatings simulations, for non-absorbing (glass) and absorbing (silicon) substrates. The rest

concerns simulations for subwavelength anti-reflective structures with various pillar shapes and arrangements.

4.4.1 Thin-film coatings on glass

In Figure 31, the reflectivity mainly across the visible range of wavelength (400 – 800 nm) is represented for bare glass with refractive index $n_g = 1.52$ (black line), for magnesium fluoride MgF_2 single-layer AR coating on glass with refractive index $n = 1.38$ and thickness $d = \lambda_t/4$, (blue line), for double-layer AR coating on glass, where the first layer is magnesium fluoride MgF_2 with refractive index $n_1 = 1.38$ and thickness $d = \lambda_t/4$, while the second layer is aluminum oxide (Al_2O_3) with refractive index $n_2 = 1.69$ and thickness $d = \lambda_t/4$ (green line) and finally, for triple-layer AR coating on glass, where the first layer is magnesium fluoride MgF_2 with refractive index $n_1 = 1.38$ and thickness $d = \lambda_t/4$, the second layer is zirconium dioxide ZrO_2 with refractive index $n_2 = 2.05$ and thickness $d = \lambda_t/2$ and the third layer is cerium trifluoride CeF_3 with refractive index $n_3 = 1.64$ and thickness $d = \lambda_t/4$ (red line).

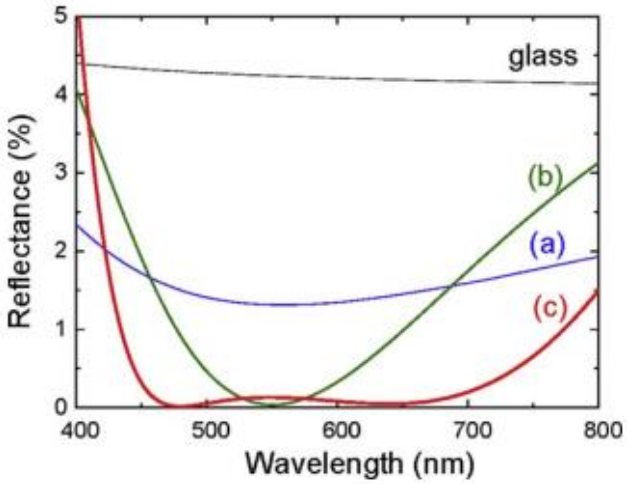

Figure 31: Reflectance as a function of wavelength for anti-reflection (AR) coatings: (a) single-layer AR coating, (b) double-layer AR coating, (c) triple-layer AR coating [39].

These parameters were taken from reference [39] and then imported to Maxima (TMM) and FDTD Solutions. The simulated reflectance is depicted in Figure 32 and Figure 33 respectively.

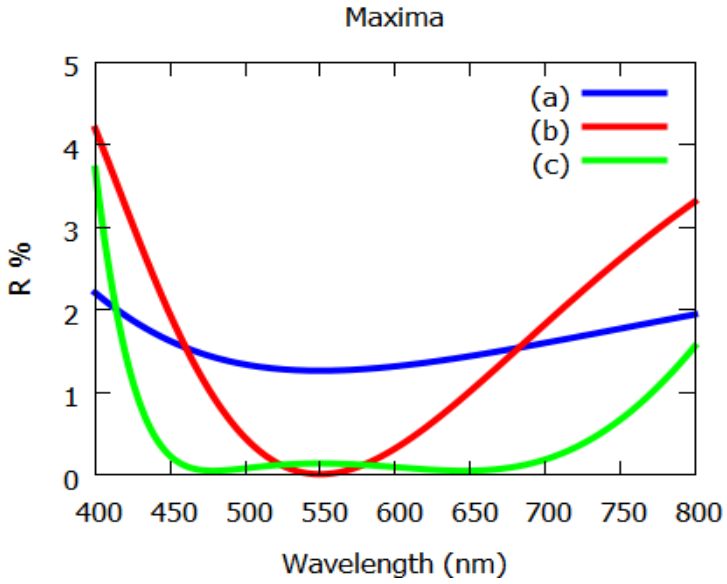

Figure 32: Maxima (TMM) simulation of reflectance as a function of wavelength for anti-reflection (AR) coatings: (a) single-layer AR coating, (b) double-layer AR coating, (c) triple-layer AR coating

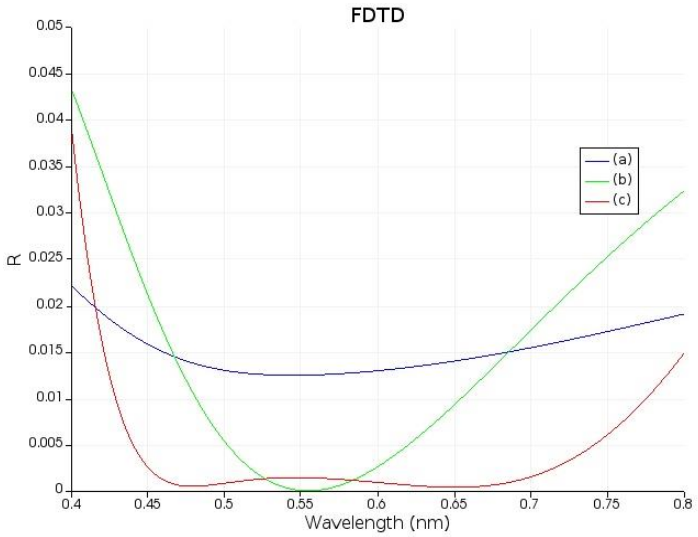

Figure 33: FDTD simulation of reflectance as a function of wavelength for anti-reflection (AR) coatings: (a) single-layer AR coating, (b) double-layer AR coating, (c) triple-layer AR coating

In Tables 2-4 the comparative results at certain wavelengths of the validation study are summarized. Table 2 includes comparison results at certain wavelengths between reference and simulation for single-layer AR coating, Table 3 for double-layer AR coating and Table 4 for

triple-layer AR coating. It is shown that there is very good correlation between reference and simulation results.

Table 2: Reflectance comparison at certain wavelengths between reference and simulation results for single-layer AR coating

(nm)	Ref.	TMM	FDTD
450	1.69%	1.59%	1.58%
600	1.32%	1.32%	1.29%
750	1.73%	1.73%	1.73%

Table 3: Reflectance comparison at certain wavelengths between reference and simulation results for double-layer AR coating

(nm)	Ref.	TMM	FDTD
450	1.93%	1.95%	2.12%
600	0.3%	0.32%	0.25 %
750	2.48%	2.58%	2.52%

Table 4: Reflectance comparison at certain wavelengths between reference and simulation results for triple-layer AR coating

(nm)	Ref.	TMM	FDTD
450	0.27%	0.23%	0.25%
600	0.08%	0.09%	0.08%
750	0.64%	0.68%	0.64%

4.4.2 Thin-film coatings on silicon

In Figure 34, the reflectivity across a wide range of wavelength (400 – 1600 nm) is represented for a single-layer AR coating on silicon with ideal refractive index and thickness, where the refractive index is $n = 2.0$ and thickness $d = 75\,nm$ at normal incidence (red line). Respectively, Figure 35 represents the reflectivity for a triple-layer AR coating on silicon with ideal refractive index and thickness, where the refractive index is $n_1 = 1.10$ and thickness

$d_1 = 136\,nm$ for the first layer, refractive index $n_2 = 1.50$ and thickness $d_2 = 100\,nm$ for the second layer and refractive index $n_3 = 2.72$ and thickness $d_3 = 55\,nm$ for the third layer at normal incidence (red line).

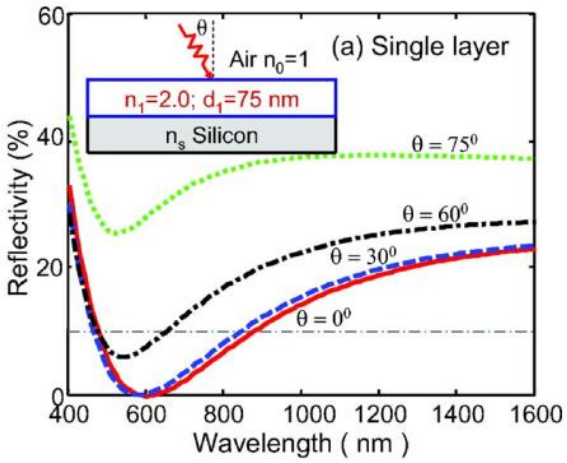

Figure 34: Reflectance of quarter wavelength single-layer AR coating with ideal indices and thicknesses [40].

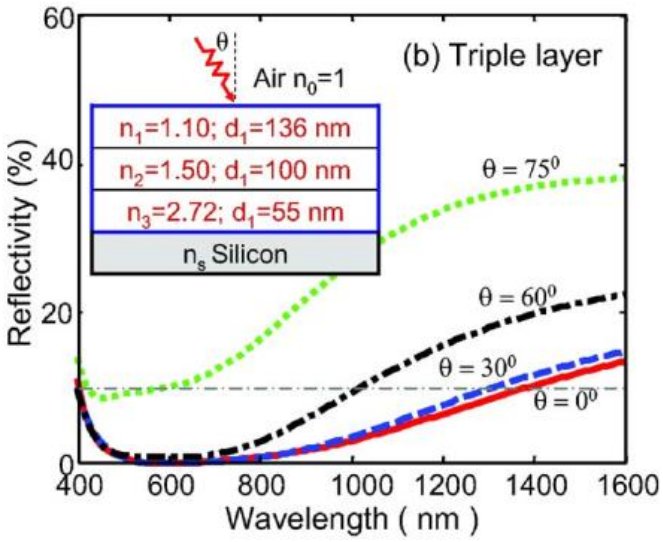

Figure 35: Reflectance of triple-layer AR coating with ideal indices and thicknesses [40].

These parameters were taken from reference [40] and then imported to FDTD Solutions. The simulated reflectance is depicted in Figure 36 for both single and triple-layer AR coatings.

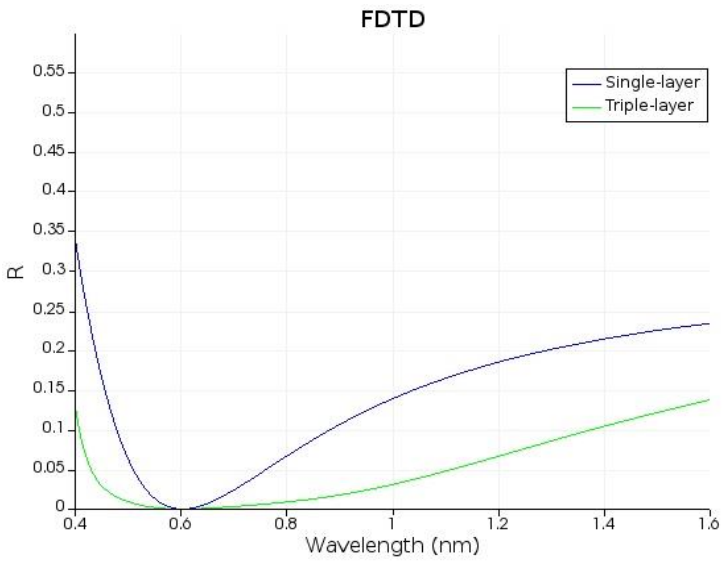

Figure 36: FDTD simulation of reflectance as a function of wavelength for single and triple-layer AR coatings on silicon substrate

In Tables 5-6 the comparative results at certain wavelengths of the validation study are summarized. Table 5 includes comparison results at certain wavelengths between reference and FDTD simulation for ideal single-layer AR coating and Table 6 for ideal triple-layer AR coating on silicon. Again, there is great correlation between reference and simulation results.

Table 5: Reflectance comparison at certain wavelengths between reference and simulation results for single-layer AR coating

(nm)	Ref.	FDTD
800	6.61%	6.75%
1100	16.87%	16.57%
1400	21.52%	21.37%

Table 6: Reflectance comparison at certain wavelengths between reference and simulation results for tripe-layer AR coating

(nm)	Ref.	FDTD
800	0.78%	0.89%
1100	4.48%	4.87%
1400	10.3%	10.51%

4.4.3 Conical and parabolic subwavelength structures on silicon substrate

From now on, the comparative validation study concerns subwavelength anti-reflective structures. In Figure 37, the reflectivity mainly across the visible range of wavelength (300 – 800 nm) is represented for nipple arrays with conical shape on glass substrate with refractive index $n_g = 1.52$. These arrays were in fact patterned on glass so they have the same refractive index. The black dashed line shows the reflectivity of flat glass, while the rest show the reflectivity with the subwavelength nipple arrays on top. For a fixed period of 200 nm, reflectivity for various heights is depicted and in particular for $h = 50\,nm$ (red line), for $h = 75\,nm$ (blue line), for $h = 100\,nm$ (green line), for $h = 150\,nm$ (pink line), for $h = 200\,nm$ (gold line) and for $h = 250\,nm$ (purple line).

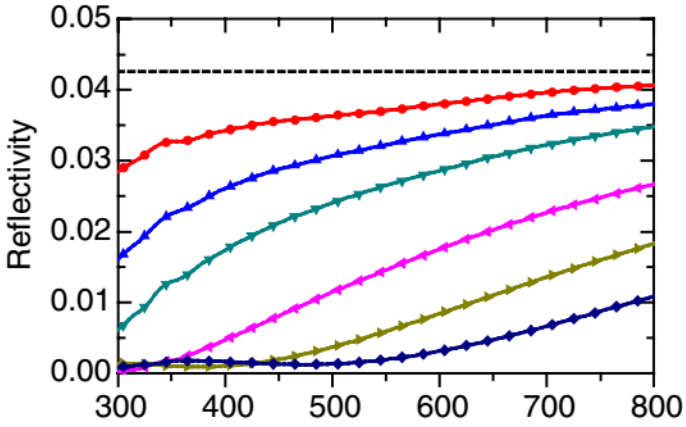

Figure 37: Reflectance as a function of wavelength from moth-eye facets covered with corneal nipple arrays with conical shape [41].

Similar study was conducted with the same parameters, but in this case nipple arrays have a parabolic shape. This is shown on Figure 38.

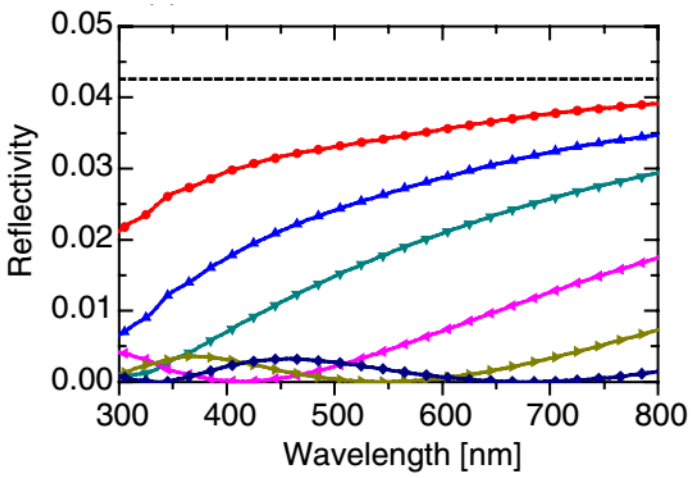

Figure 38: Reflectance as a function of wavelength from moth-eye facets covered with corneal nipple arrays with parabolic shape [41].

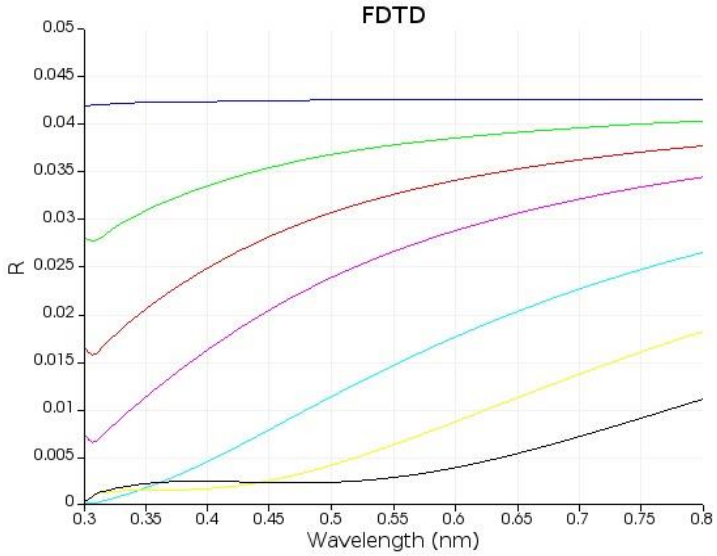

Figure 39: FDTD simulation of reflectance as a function of wavelength of moth-eye nipple array with conical shape at different heights.

Then, the exact same parameters were taken from reference [40] and were imported to FDTD Solutions. The simulated reflectance of conical nipple arrays is depicted in Figure 39 and the reflectance of parabolic nipple arrays in Figure 40.

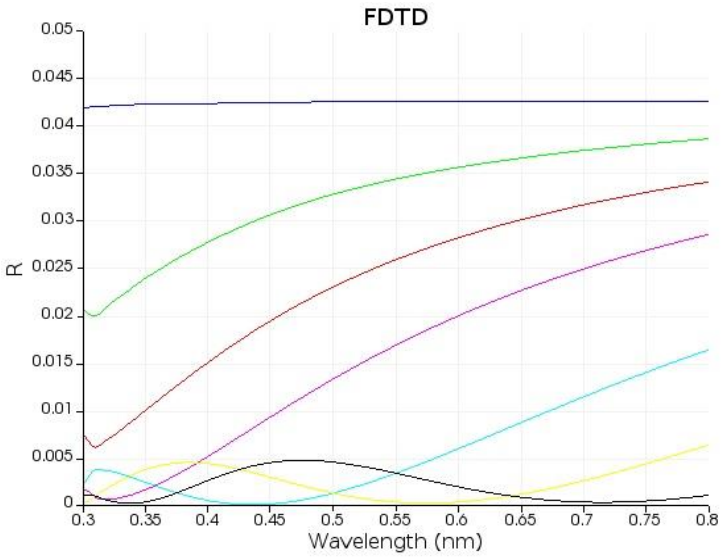

Figure 40: FDTD simulation of reflectance as a function of wavelength of moth-eye nipple array with parabolic shape at different heights.

Table 7: Reflectance comparison at certain wavelengths between reference and simulation results for moth-eye nipple arrays with conical shape.

Cone Ref./FDTD	h=50nm	h=75nm	h=100nm	h=150nm	h=200nm	h=250nm
400	3.42%/ 3.35%	2.55%/ 2.49%	1.73%/ 1.69%	0.47%/ 0.45%	0.10%/ 0.16%	0.15%/ 0.14%
500	3.63%/ 3.68%	3.06%/ 3.08%	2.4%/ 2.39%	1.14%/ 1.14%	0.37%/ 0.41%	0.14%/ 0.23%
600	3.79%/ 3.85%	3.39%/ 3.41%	2.85%/ 2.88%	1.75%/ 1.76%	0.85%/ 0.87%	0.32%/ 0.38%
700	3.95%/ 3.96%	3.62%/ 3.63%	3.21%/ 3.22%	2.26%/ 2.27%	1.35%/ 1.38%	0.69%/ 0.73%

In Tables 7-8 the comparative results at certain wavelengths of the validation study are summarized. Table 7 includes comparison results at certain wavelengths between reference and FDTD simulation for conical nipple arrays and Table 8 for parabolic nipple arrays. It is clearly shown that there is great agreement between reference and simulation results.

Table 8: Reflectance comparison at certain wavelengths between reference and simulation results for moth-eye nipple arrays with parabolic shape.

Parabola Ref./FDTD	h=50nm	h=75nm	h=100nm	h=150nm	h=200nm	h=250nm
400	2.95%/ 2.78%	1.75%/ 1.51%	0.68%/ 0.52%	0.03%/ 0.05%	0.31%/ 0.43%	0.22%/ 0.26%
500	3.34%/ 3.28%	2.42%/ 2.31%	1.48%/ 1.34%	0.21%/ 0.13%	0.08%/ 0.12%	0.26%/ 0.45%
600	3.55%/ 3.56%	2.88%/ 2.82%	2.10%/ 2%	0.71%/ 0.62%	0.03%/ 0.03%	0.10%/ 0.19%
700	3.77%/ 3.74%	3.23%/ 3.17%	2.58%/ 2.49%	1.26%/ 1.16%	0.32%/ 0.26%	0.02%/ 0.03%

4.4.4 Pyramidal subwavelength structure on silicon substrate

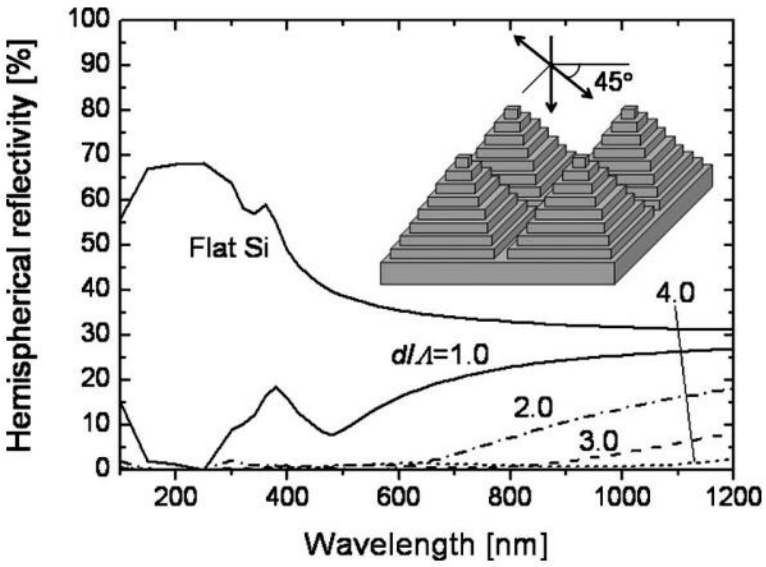

Figure 41: Calculated spectral reflectivity of two-dimensional Si pyramid gratings with a periodicity Λ of 100 nm for several aspect ratios d/Λ=1.0, 2.0, 3.0, and 4.0. [42]

In Figure 41, the reflectivity across a wide range of wavelength (200 – 1200 nm) is represented for subwavelength pyramidal rectangular structure on silicon substrate. These arrays were in fact patterned on silicon so they have the same refractive index. The simulations of this reference were conducted via rigorous coupled wave analysis (RCWA) so in this case, the validity between the two methods, FDTD and RCWA, is examined. The pyramids are constructed in the same way as in the reference, constituted from an eight-layer stack. The diagram involves the reflectivity of bare Si and then, the reflectivity of the subwavelength structures with fixed period $\Lambda = 100\,nm$ and various heights (d), thus changing the aspect ratio d/Λ. Then, the exact same parameters were taken from reference [42] and were imported to FDTD Solutions. The simulated reflectance of bare Si and pyramidal subwavelength structures with different aspect ratios is depicted in Figure 42.

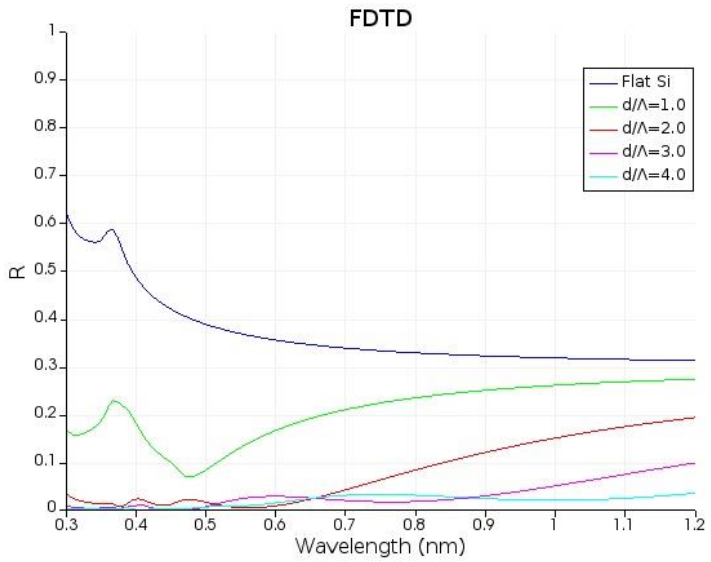

Figure 42: FDTD simulation of reflectance as a function of wavelength of a subwavelength pyramidal structure with fixed period (Λ) of 100 nm at different heights (d).

Table 9: Reflectance comparison at certain wavelengths between reference and simulation results for bare Si

(nm)	Ref.	FDTD
500	38.67%	38.88%
700	33.9%	33.95%
900	32.11%	32.35%

Table 10: Reflectance comparison at certain wavelengths between reference and simulation results for a subwavelength pyramidal structure with aspect ratio d/Λ=1.0

(nm)	Ref.	FDTD
500	8.98%	8.43%
700	20.31%	20.89%
900	24.44%	25.23%

In Tables 9-12 the comparative results at certain wavelengths of the validation study are summarized. Table 9 includes comparison results at certain wavelengths between reference and FDTD simulation for bare Si, Table 10 for an aspect ratio d/Λ=1.0, Table 11 for an aspect ratio d/Λ=2.0 and Table 12 for an aspect ratio d/Λ=3.0. For an aspect ratio d/Λ=4.0, it was not able to extract any data from the reference diagram. Again, it is shown that there is fine agreement between reference and simulation results and in between the methods also.

Table 11: Reflectance comparison at certain wavelengths between reference and simulation results for a subwavelength pyramidal structure with aspect ratio d/Λ=2.0

(nm)	Ref.	FDTD
800	6.93%	8.37%
1000	13.23%	15.13%

Table 12: Reflectance comparison at certain wavelength between reference and simulation results for a subwavelength pyramidal structure with aspect ratio d/Λ=3.0

(nm)	Ref.	FDTD
1100	5.5%	5.13%

4.4.5 Hexagonal parabolic structure on silicon substrate

In Figure 43, the reflectivity across a wide range of wavelength (400 – 900 nm) is represented for subwavelength parabolic structure on silicon substrate. This array is in fact patterned on silicon so they have the same refractive index. The silicon protuberances are arranged in hexagonal lattice with a period of 510 nm, base diameter 470 nm and 800 nm height.

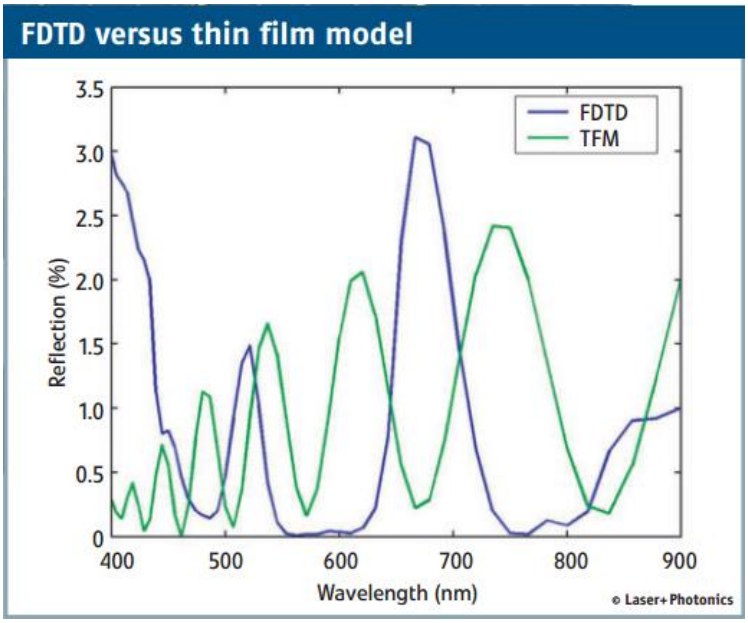

Figure 43: Calculated reflectance from silicon wafer etched with a moth-eye pattern as calculated by FDTD Solutions (blue line) and an effective medium thin film model (green line) [44].

The simulated reflectance of the parabolic subwavelength structures with different aspect ratios is represented in Figure 44 and in Table 13 the validation comparison results at certain wavelengths between reference and FDTD simulation are shown.

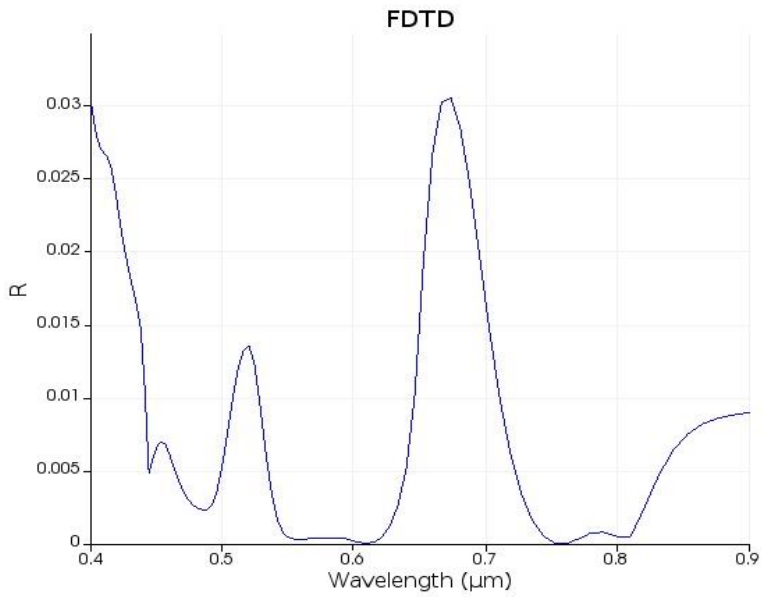

Figure 44: FDTD simulation of reflectance as a function of wavelength from the hexagonal parabola array with a period of 510 nm, 470 nm base diameter and 800 nm height.

Table 13: Reflectance comparison at certain wavelengths between reference and simulation results for silicon hexagonal parabola array

(nm)	Ref.	FDTD
500	0.49%	0.55%
600	0.03%	0.02%
650	1.68%	1.6%
700	1.77%	1.63%
800	0.09%	0.06%
850	0.82%	0.74%

4.5 Simulation using a cicada wing bio-template

After we verified the validity of the results of the method with those of the bibliography, now we can proceed to novel simulations in order to create an optimized subwavelength anti-reflection scheme based on the cicada wing nano-nipple array. The anti-reflection properties of the nipple arrays were investigated by varying the morphological and topographical specifications of the protuberances.

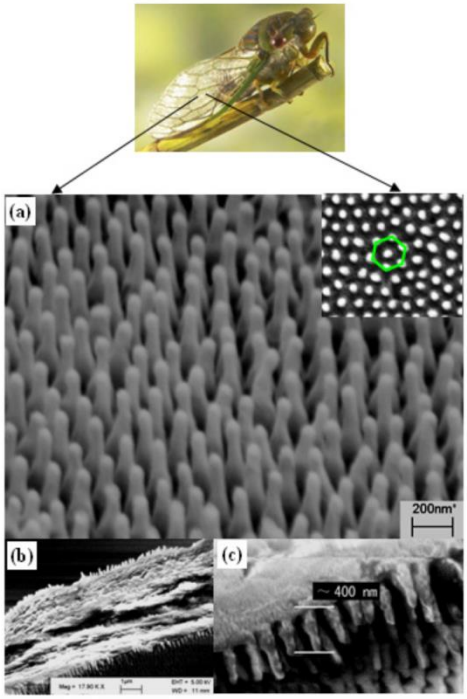

Figure 45: SEM images of a cicada wing. (a) Large-scale perspective view. The inset is a top view. (b) Cross-sectional view showing the dorsal and ventral surfaces full of nano-nipples. (c) Higher-magnification cross-sectional view. [46]

Figures 45(a) and 45(b) show typical SEM images of the wing dorsal surface morphology of a cicada (Cryptympana atrata Fabricius). The transparent wing surface contains a hexagonally quasi-two-dimensional (q2D) ordered assembly of nano-nipples. The nearest-neighbor nipple distance is approximately 190 nm, as derived from the top view of an SEM image (the inset of Figure 45(a)). According to the cross-sectional image of Figure 45(c), each of the nipples has a height of around 400 nm, and average diameters of about 150 nm at the nipple base. The antireflection function of the wing associated with camouflage is achieved by these

subwavelength nipple arrays, which effectively introduce a gradual refractive index profile at the interface between wing and air, and reduce the reflectivity over broad angle range.

4.5.1 Bio-template simulation

Nearly all variables related to the morphological and topographical specification of cicada wing features affect the reflectance of the structure (i.e. fill factor, shape, height, period). To compare the effect of each of the basic design parameters, first and foremost it was needed to simulate the cicada wing nano-structure with the exact same characteristic as a bio-template. The parabolic shape of the pillars was used because it was considered to closely approximate the features found on the real cicada wing. With that being said, it can be seen in Figure 46 the reflectance as a function of wavelength for flat (blue line) and cicada wing biomimetic patterned PMMA.

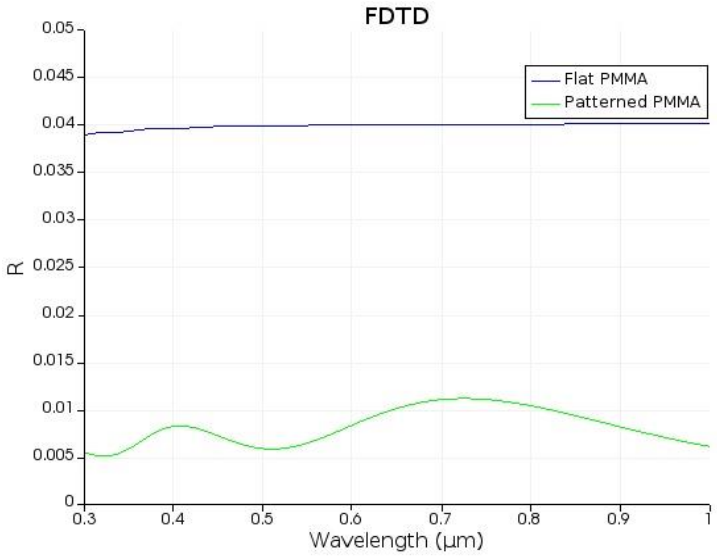

Figure 46: FDTD simulation of reflectance as a function of wavelength for flat (blue line) and cicada wing biomimetic patterned PMMA

4.5.2 Fill factor

The first parameter that needs to be investigated is the fill factor. The original fill factor of the cicada wing with nipple base diameter of 150 nm and period of 190 nm equals to 0.79. Figure 47 shows the reflectance spectra as a function of wavelength for different fill factors. The

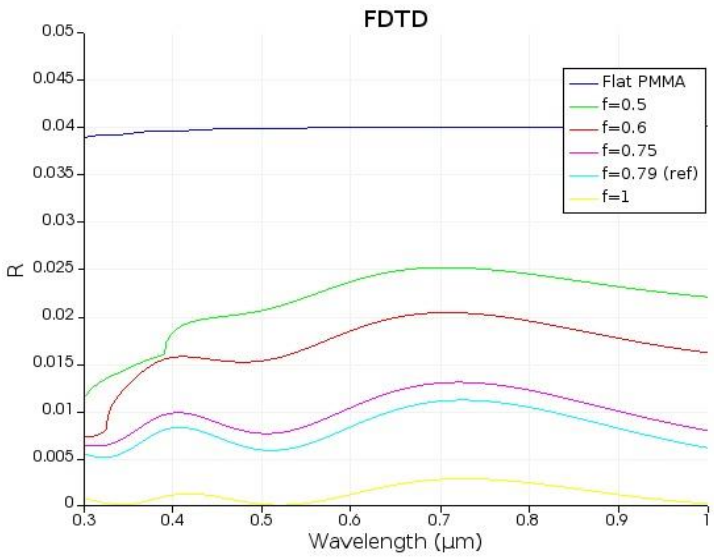

Figure 47: FDTD simulation of reflectance as a function of wavelength for different fill factors

fill factor is calculated as the fraction of nipple base diameter by the period. The nipple base diameter remains constant at 150 nm, while the period changes resulting in different fill factors. The best anti-reflective results are given by fill factor equal to 1 as it is reasonable, and this investigation is continued using this specific fill factor.

4.5.3 Arrangement ways for different pillar style

After the fill factor optimization, the next step that needs to be investigated is the pillar shape along with the way of arrangement. The nipple arrays were investigated by varying the shape of the protuberances, in cones, parables and pyramids, and by varying the way of arrangement in rectangular or hexagonal order.

4.5.3.1 Cone

In Figure 48, the reflectivity as a function of wavelength is represented for conical shape of pillars in a rectangular and hexagonal arrangement. It is observed that a hexagonally arranged array achieves significantly lower reflectivity across the whole range of the simulation spectrum. Figure 49 and 50 show the arrangement of rectangular and hexagonal array as it looks in the FDTD Solutions simulation window.

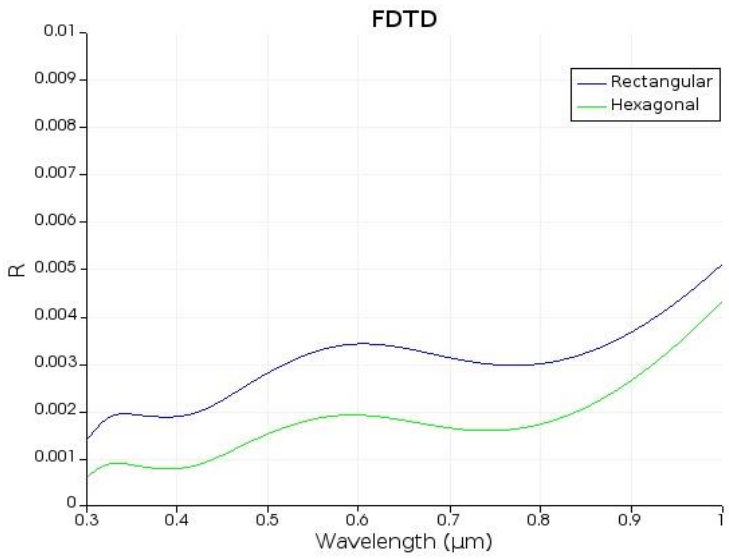

Figure 48: FDTD simulation of reflectance as a function of wavelength for a rectangular and hexagonal conical array

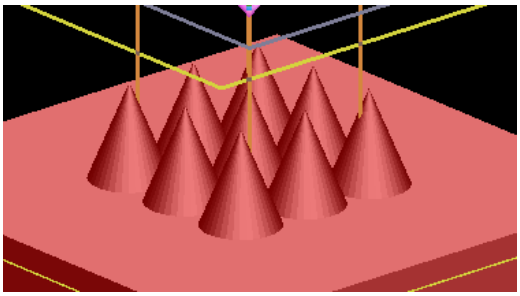

Figure 49: Simulation window image of the rectangular conical array

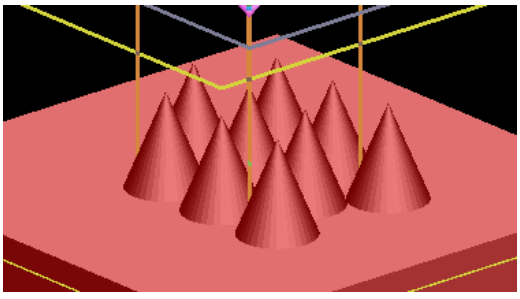

Figure 50: Simulation window image of the hexagonal conical array

4.5.3.2 Parabola

In Figure 51, the reflectivity as a function of wavelength is represented for parabolic shape of pillars in a rectangular and hexagonal arrangement. It is observed that a hexagonally arranged array achieves significantly lower reflectivity across the whole range of the simulation spectrum. Figure 52 and 53 show the arrangement of rectangular and hexagonal array as it looks in the FDTD Solutions simulation window.

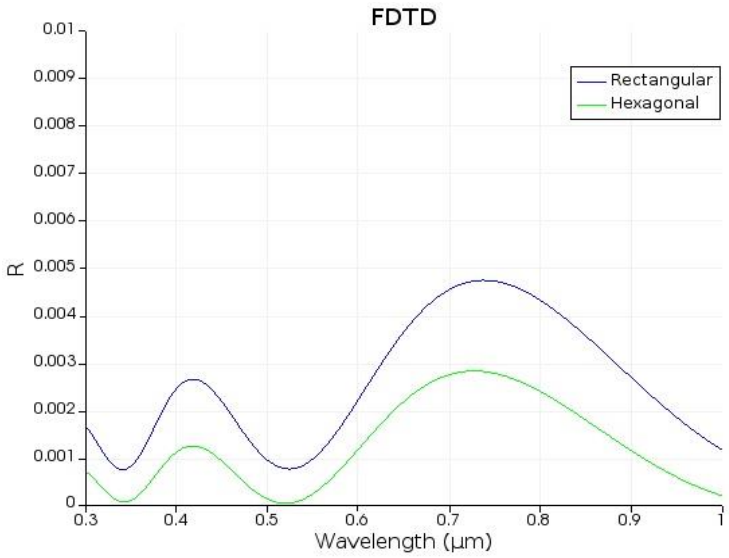

Figure 51: FDTD simulation of reflectance as a function of wavelength for a rectangular and hexagonal parabolic array

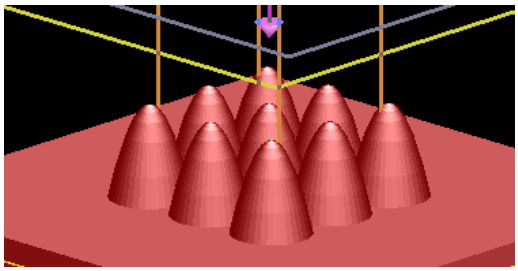

Figure 52: Simulation window image of the rectangular parabolic array

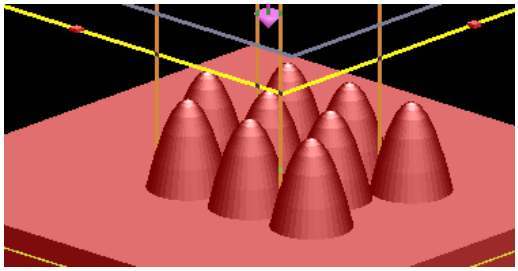

Figure 53: Simulation window image of the hexagonal parabolic array

4.5.3.3 Pyramid

In Figure 54, the reflectivity as a function of wavelength is represented for pyramidal shape of pillars in a rectangular and hexagonal arrangement. It is observed that the arrangement way, either rectangular or hexagonal, does not have a great impact in reflectivity. Figure 55 and 56 show the arrangement of rectangular and hexagonal array as it looks in the FDTD Solutions simulation window.

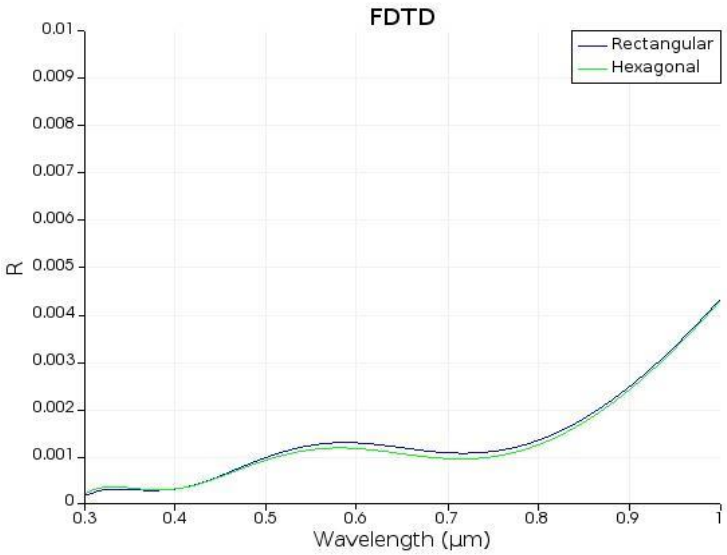

Figure 54: FDTD simulation of reflectance as a function of wavelength for a rectangular and hexagonal pyramidal array

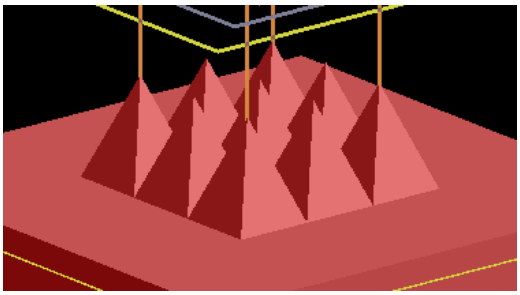

Figure 55: Simulation window image of the rectangular pyramidal array

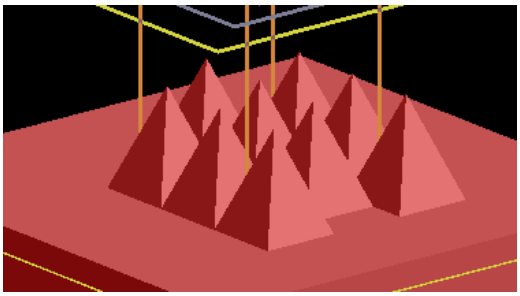

Figure 56: Simulation window image of the hexagonal pyramidal array

4.5.4 Changing geometrical features

It is evident that by tuning the pillar height and period, we can optimize the antireflective properties of a subwavelength structured surface for a specific part of the spectrum. Therefore, it is possible to tailor the nano-array design for optimum performance as an anti-reflection scheme. Until now we have concluded the optimal parameters are the fill factor to be equal to 1 and the hexagonal arrangement of the pillars and we have decided to move on with parabolic pillar shape. So the last part contains the investigation of height and period differentiation.

4.5.4.1 Fixed period

Figure 57 presents the reflectivity as a function of wavelength with fixed period of 150 nm, as the base diameter of the protuberances found on the cicada wing, and height of 200 nm (blue line), 300 nm (green line), 400 nm (red line), 500 nm (pink line) and 600 nm (cyan line). It is obvious that as the period increases, the low reflectance band broadens and shifts to longer wavelengths.

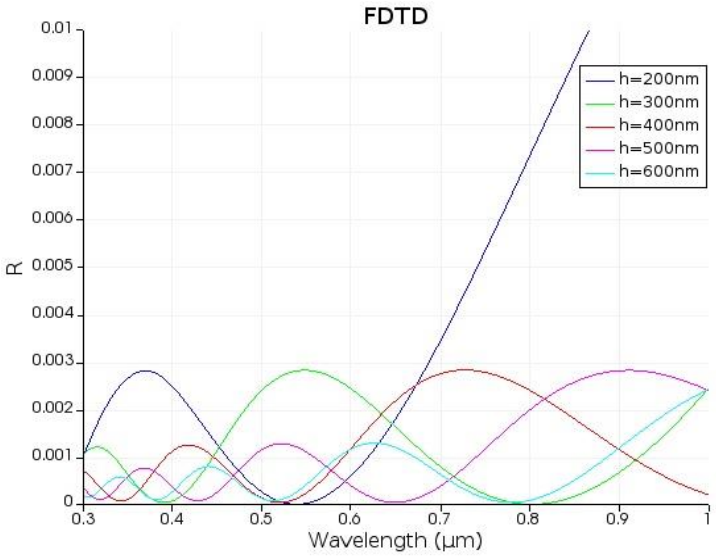

Figure 57: FDTD simulation of reflectance as a function of wavelength for the cicada wing biomimetic structure with parabolic pillars in hexagonal array with a fixed period of 150 nm at various heights

4.5.4.2 Fixed height

Further simulations were conducted to analyze the effects of changing pillar period. Figure 58 presents the reflectivity as a function of wavelength with fixed height of 400 nm, as the height of the protuberances found on the cicada wing, and period of 50 nm (blue line), 100 nm (green line), 150 nm (red line), 200 nm (pink line) and 250 nm (cyan line). It is shown that in the period range between 100 nm and 300 nm there is no significant change in peak reflectivity (0.27% - 0.29%), except the case where the period is 50 nm that we observe a slight increase in peak reflectivity (0.33%).

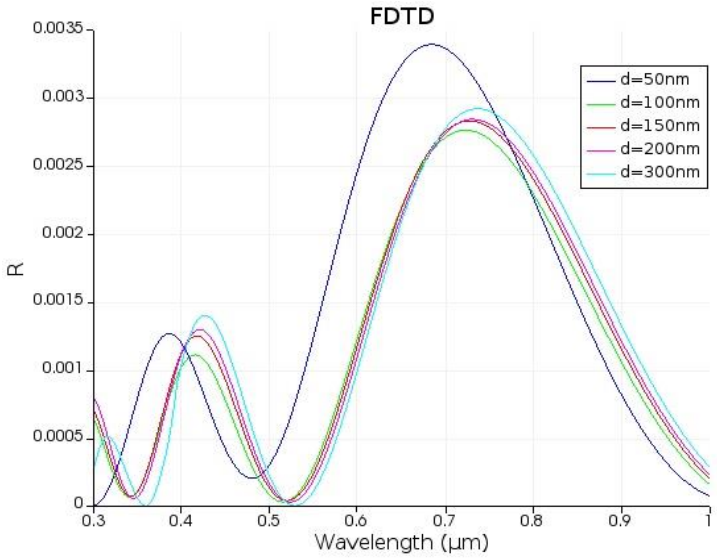

Figure 58: FDTD simulation of reflectance as a function of wavelength for the cicada wing biomimetic structure with parabolic pillars in hexagonal array with a fixed height of 400 nm at various periods

4.6 Simulation expanding on a thin organic solar cell

After completing the optimization of the cicada wing subwavelength structures, we progress through the last part of the experimental part which is the addition of the structure at a thin organic solar cell (OSC). The OSC that is considered in this work is retrieved from reference [48] and is constructed with a PET (polyethylene terephthalate) flexible substrate with 1.4 μm thickness, a PEDOT:PSS (poly(3,4-ethylenedioxythiophene) polystyrene sulfonate) with 150 nm thickness, a P3HT:PCBM active layer with 200 nm thickness and a 115 nm thick Ag electrode (Figure 59).

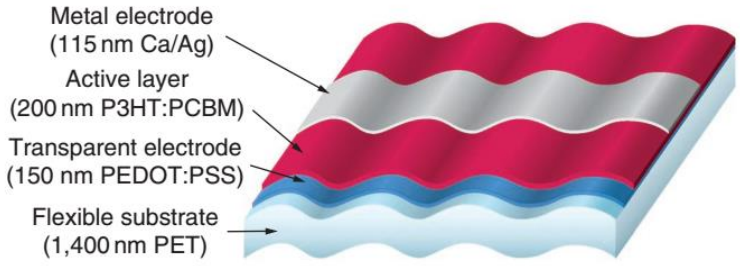

Figure 59: Scheme of the sub-2μm thick and flexible organic solar cell

The optical data that used for setting up the simulation parameters, for each material, is retrieved from bibliography and can be found in Chapter 4.3. The parameters of the subwavelength anti-reflective structure are the following; 400 nm height, 200 nm base diameter and 200 nm period which results in fill factor that equals 1 and the protuberances are arranged in a hexagonal lattice. The first simulation that was carried out is about the thin organic solar cell without the back metal electrode in order to avoid extra reflection and acquire a first impression of the reflectivity. In Figure 61, it is shown the reflectivity as a function of wavelength for the OSC without the Ag electrode, with (green line) and without (blue line) the anti-reflective structure and apparently the subwavelength anti-reflective structure lead to much lower reflectance.

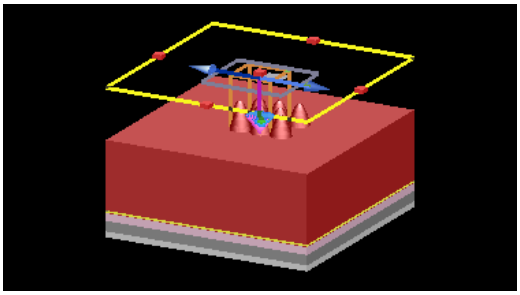

Figure 60: Simulation window image of a complete thin-film organic solar cell patterned with the cicada wing biomimetic structure

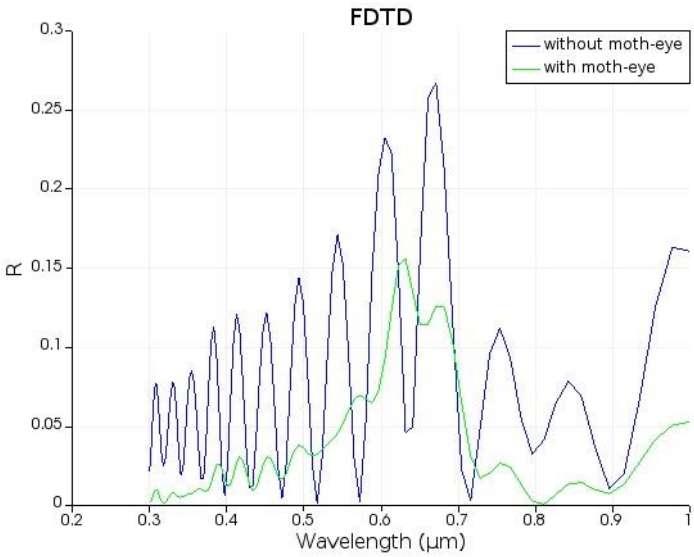

Figure 61: FDTD simulation of reflectance as a function of wavelength of a thin-film organic solar cell without Ag cathode

Figure 61 represents the reflectivity as a function of wavelength for the OSC without the subwavelength biomimetic structure with (green line) and without (blue line) the Ag electrode.

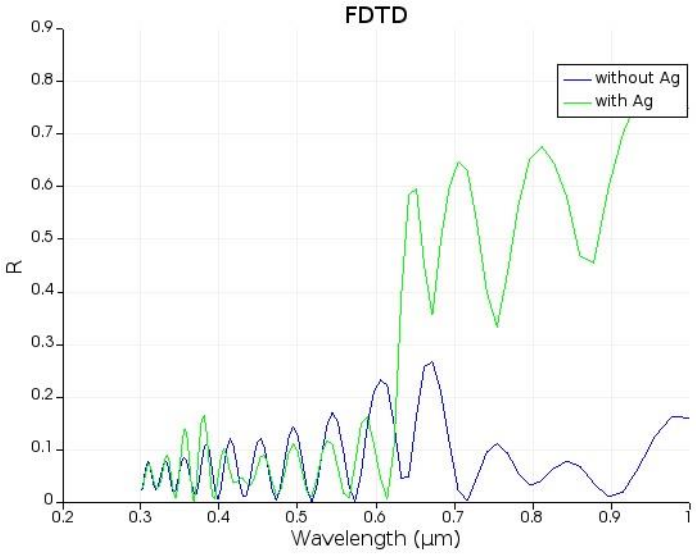

Figure 62: FDTD simulation of reflectance as a function of wavelength of a thin-film organic solar cell without the cicada wing biomimetic structure

Figure 62 represents the reflectivity as a function of wavelength for the OSC with the subwavelength biomimetic structure with (green line) and without (blue line) the Ag electrode.

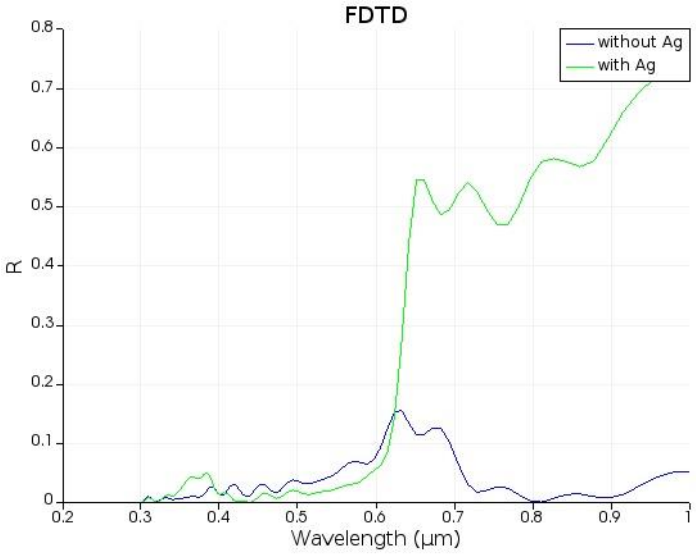

Figure 63: FDTD simulation of reflectance as a function of wavelength of a thin-film organic solar cell with the cicada wing biomimetic structure

Finally, in Figure 64 is presented an integrated comparison of the reflectivity as a function of wavelength for a complete OSC with (green line) and without (blue line) the subwavelength biomimetic structure and in Figure 65 a more specific image is displayed with respect to the visible wavelength.

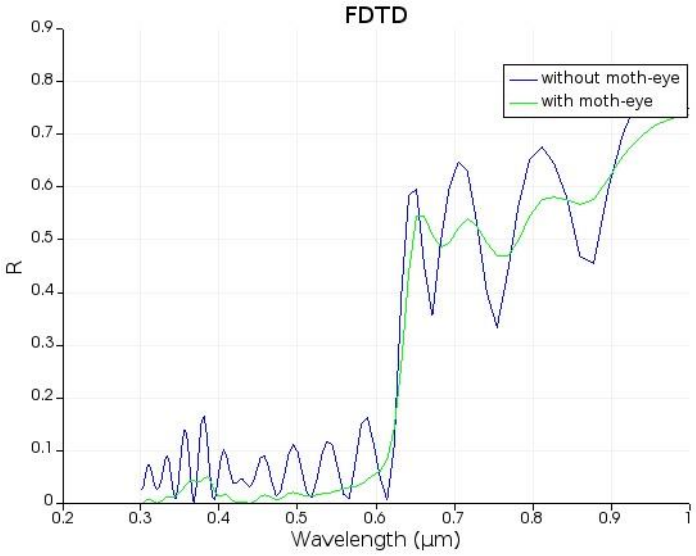

Figure 64: FDTD simulation of reflectance as a function of wavelength of a complete thin-film organic solar cell with and without the cicada wing biomimetic structure

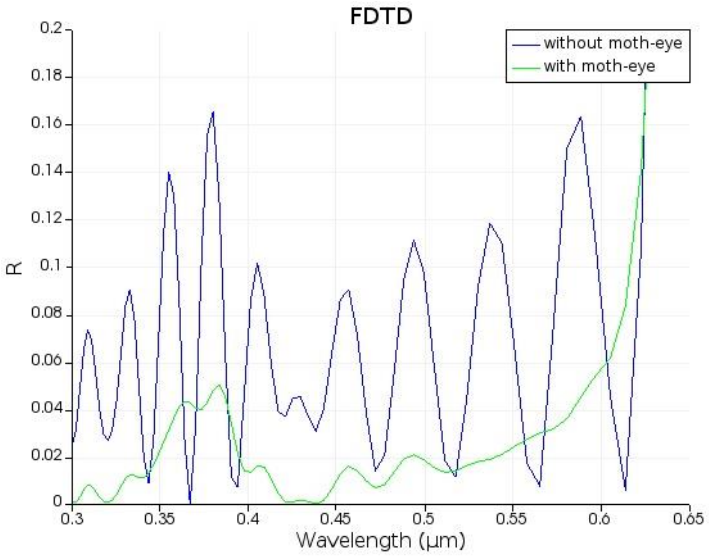

Figure 65: FDTD simulation of reflectance as a function of wavelength in the visible region of a thin-film organic solar cell with and without the cicada wing biomimetic structure

5 Chapter 5 – Discussion and conclusions

5.1 Results

In this thesis an investigation of the reflection of subwavelength anti-reflection structures has taken place by FDTD simulations. These structures were considered, using the structure found on the cicada wing as a bio-template and further research was conducted, on how the morphological and topographical specifications of cicada wing features affect the reflectance of the structure. Then, the cicada wing structure was adapted on the surface of a novel thin organic solar cell and a significant reduction in reflectance was proven.

To accurately and fairly assess novel forms of antireflection, it is important to have an understanding of how effective the more traditional methods, when optimized, can be. Therefore, a detailed approach to refractive index selection and optimization of the thickness of thin-film anti-reflection coatings was carried out. In order to achieve this, a powerful tool was created by writing a script in Maxima using the transfer matrix method (TMM).

However, these more traditional AR methods are being challenged by subwavelength-scale texturing, inspired by moth-eye AR surfaces found in Nature. Reports show that subwavelength-scale texturing on practically any investigated substrate can significantly outperform other types of AR across a wide range of wavelengths.

This approach was then adapted to model subwavelength arrays simulations found in bibliography, in order to conduct a comparative study and validate that the FDTD simulations are properly set up and the results are accurate. Then, using the structure found on the cicada wing as a bio-template, was shown that reflectance is heavily influenced by the period of the array as well as the height and shape of the individual pillars alongside their arrangement way.

So, subwavelength texturing in the form of artificial ‘moth-eye’ arrays is a promising alternative to thin-film ARCs for reducing reflectance from the top surface of solar cells. In this last part of the dissertation, a novel thin organic solar cell was considered and a significant reduction in reflectance was proven.

Aside from the photovoltaic applications focused on in this study, ‘moth-eye’ arrays could be useful in other technologies where reflectance needs to be minimized. Photodetectors in military

applications, for which signal strength is vital to performance, may be improved by the use of a ‘moth-eye’ array on the front surface, carefully designed to minimize reflectance for the wavelength range of interest. The stealth properties of such devices would also be improved by coating the reflective surface with a moth-eye array. Subwavelength AR coatings could also be used to reduce glare from screens and lenses for both military and civilian technologies.

In conclusion, the main contributions of this work are firstly a thorough analysis of the factors to consider in the design of thin-film anti-reflection coatings and the development of a new simulation tool developed in Maxima using transfer matrix method (TMM). Secondly, this study provides an in-depth assessment, through simulations, of the optical performance of subwavelength biomimetic structures, in terms of morphological characteristics and their applicability to solar cells. This demonstrates that such surfaces can transmit more light than surfaces with traditional AR schemes and so can potentially be of great benefit to photovoltaics.

5.2 Suggested future work

Devices such as photodetectors and solar cells could benefit considerably from being integrated into subwavelength-nipple anti-reflection structures. For solar cells specifically, constructing the active layer within the nipple structure which is used for antireflection, reduces the distance the electron-hole pairs would have to travel before being absorbed by the contacts and as a result reduces the chance of recombination of the charge carriers in the bulk. This improves device efficiency substantially which allows the cell to use less material to achieve similar efficiencies to flat architectures using the same materials. Also, if this design is applied to photodetectors, it would also increase their sensitivity as more carriers would be collected at low light levels due to the more efficient design.

Bibliography

[1]. Hecht, Eugene. Optics. 4th Edition, Mass: Addison-Wesley, 2002. ISBN 0-321-18878-0

[2]. Stavroulakis, P. I. (2012), "Fabrication and characterization of biomimetic antireflective surfaces with reduced glare", University of Southampton, Faculty of Physical and Applied Sciences, PhD Thesis, 225

[3]. Zhang, C., Hao, Y., & Chen, D. (n.d.). World's largest Science, Technology & Medicine Open Access book publisher 'Investigation of Organic Bulk Heterojunction Solar Cells from Optical Aspect'.

[4]. Yu, G., Gao, J., Hummelen, J. C., Wudl, F., & Heeger, A. J. (1995). Polymer photovoltaic cells: enhanced efficiencies via a network of internal donor-acceptor heterojunctions. Science, 270(5243), 1789-1791.

[5]. Pacios, R., Chatten, A. J., Kawano, K., Durrant, J. R., Bradley, D. D. C., & Nelson, J. (2006). Effects of photo-oxidation on the performance of poly [2-methoxy-5-(3′,7′-di-methyloctyloxy)-1, 4-phenylene vinylene]:[6,6]-phenyl C61-butyric acid methyl ester solar cells. *Adv. Funct. Mater*, 16(10), 2117-2126.

[6]. Park, S. H., Roy, A., Beaupre, S., Cho, S., Coates, N., Moon, J. S., Moses, D., Leclerc, M., Lee, K., & Heeger, A. J. (2009). Bulk Heterojunction Solar Cells With Internal Quantum Efficiency Approaching 100%. *Nature Photonics*, 3, 297-303.

[7]. P. T. Landsberg and V. Badescu. Solar energy conversion: list of efficiencies and some theoretical considerations. *Prog. Quantum Electronics*, 22:211–230 and 231–255, 1998.

[8]. Boden, S. A. (2009), "Biomimetic nanostructured surfaces for antireflection in photovoltaics", University of Southampton, Faculty of Engineering, Science & Mathematics, PhD Thesis, 256.

[9]. W. Shockley and H. J. Queisser. Detailed balance limit of efficiency of p-n junction solar cells. *J. Appl. Phys*, 32(3)

[10]. C. M. Chong, S. R. Wenham, and M. A. Green. High-efficiency, laser grooved, buried contact silicon solar cells. *Appl. Phys. Lett.*, 52(5):407–409, 1987.

[11]. M. D. Lammert and R. J. Schwartz. The interdigitated back contact solar cell: A silicon solar cell for use in concentrated sunlight. IEEE Trans. Electron. Dev., ED-24(4):337–342,

1977

[12]. M. A. Green. High Efficiency Silicon Solar Cells. Trans Tech Publications Ltd., Aedermannsdorf, 1987.

[13]. D. H. Raguin and G. M. Morris. Antireflection structured surfaces for the infrared spectral region. *Appl. Opt.*, 32(7):1154–1167, 1993.

[14]. C.G. Bernard. Structural and functional adaptation in a visual system. Endeavour, 26:79–84, 1967.

[15]. P.B. Caplam and M. C. Hutley. Reduction of the lends reflection by the moth-eye principle. Nature, 244:281–282, 1973.

[16]. S.A. Boden and D.M. Bagnall. Tunable reflection minima of nanostructured antireflective surfaces. Applied Physics Letters, 93:133108, 2008.

[17]. S.J. Wilson and M.C. Hutley. The optical properties of 'moth-eye' antireflection surfaces. Optica Acta, 29:993–1009, 1982.

[18]. W. H. Southwell. Gradient-index antireflection coatings. Optics Letters, 8:584586, 1983.

[19]. Han, K., & Chang, C.-H. (2014). Numerical Modeling of Sub-Wavelength Anti-Reflective Structures for Solar Module Applications. Nanomaterials, 4(1), 87–128.

[20]. Yee, K.S. Numerical solution of initial boundary value problems involving maxwell's equations in isotropic media. IEEE Trans. Antennas Propag. 1966, 14, 302–307.

[21]. Taflove, A.; Brodwin, M.E. Numerical-solution of steady-state electromagnetic scattering problems using time-dependent maxwells equations. IEEE Trans. Microw. Theory Tech. 1975, 23, 623–630.

[22]. Taflove, A.; Hagness, S.C. Computational Electrodynamics: The Finite-Difference Time-Domain Method, 3rd ed.; Artech House, Inc.: Norwood, MA, USA, 2005.

[23]. Bouffaron, R.; Escoubas, L.; Simon, J.J.; Torchio, P.; Flory, F.; Berginc, G.; Masclet, P. Enhanced antireflecting properties of micro-structured top-flat pyramids. Opt. Express 2008, 16, 19304–19309.

[24]. M. Totzeck, W. Ulrich, A. Gohnermeier, and W. Kaiser. Semiconductor fabrication: Pushing deep ultraviolet lithography to its limits. Nature Photonics, 1:629–631, 2007.

[25]. L.R Harriot. Limits of lithography. Proceedings of IEEE, 89(4):366–374, 2001.

[26]. E.-B. Kley and B. Schnabel. E-beam lithography: a suitable technology for fabrication of

high-accuracy 2d and 3d surface profiles. Proceedings of SPIE, 2640:71–80, 1995.

[27]. M. D. Austin, H. Ge, W. Wu, M. Li, Z. Yu, D. Wasserman, S. A. Lyon, and S. Y. Chou. Fabrication of 5nm linewidth and 14nm pitch features by nanoimprint lithography. Applied Physics Letters, 84(26):5299–5301, 2004.

[28]. G. Hubbard, et al.. Wafer-scale transfer of nan ˇ oimprinted patterns into silicon substrates. Physica E: Low-dimensional Systems and Nanostructures, 41(6):1118–1121, 2009.

[29]. Schneider, J. B., "Introduction to the Finite Difference Time-Domain method: FDTD in 1D," Lecture materials for EE 535, Chap. 3, WSU, 2007, pp. 34-35.

[30]. Tuerxunjiang, A. (2008), "FDTD measurement of the reflection coefficient associated with total internal reflection from gainy lorentzian media", Washington State University, Department of Physics and Astronomy, Master Thesis, 68

[31]. *Wavelength*. Retrieved from https://en.wikipedia.org

[32]. *Reflection*. Retrieved from http://hyperphysics.phy-astr.gsu.edu/hbase/hframe.html

[33]. *Maxima*. Retrieved from http://maxima.sourceforge.net/index.html

[34]. D. E. Aspnes and J. B. Theeten (1980) "Spectroscopic Analysis of the Interface Between Si and Its Thermally Grown Oxide" J. Electrochem. Soc., Volume 127, Issue 6, pp. 1359-1365.

[35]. Beadie, G., Brindza, M., Flynn, R. A., Rosenberg, A., & Shirk, J. S. (2015). Refractive index measurements of poly (methyl methacrylate) (PMMA) from 0.4–1.6 μm. Applied Optics, 54(31), 139–143.

[36]. F. Monestier et al., Sol. Energy Mater. Sol. Cells 91 (2007) 405.

[37]. J. R. Tumbleston et al., Proc. of SPIE 7047, 70470S (2008).

[38]. E. D. Palik, ed., Handbook of Optical Constants of Solids, (Academic Press, 1998).

[39]. Chattopadhyay, S., Huang, Y. F., Jen, Y. J., Ganguly, A., Chen, K. H., & Chen, L. C. (2010). Anti-reflecting and photonic nanostructures. Materials Science and Engineering R: Reports, 69(1–3), 1–35.

[40]. Zhou, W., Tao, M., Chen, L., & Yang, H. (2007). Microstructured surface design for omnidirectional antireflection coatings on solar cells. Journal of Applied Physics, 102(10).

[41]. Dewan, R., Fischer, S., Benno Meyer-Rochow, V., Özdemir, Y., Hamraz, S., & Knipp, D. (2012). Studying nanostructured nipple arrays of moth eye facets helps to design better

thin film solar cells. Bioinspiration and Biomimetics, 7(1).

[42]. Sai, H., Fujii, H., Arafune, K., Ohshita, Y., Yamaguchi, M., Kanamori, Y., & Yugami, H. (2006). Antireflective subwavelength structures on crystalline Si fabricated using directly formed anodic porous alumina masks. Applied Physics Letters, 88(20), 6–9.

[43]. H. L. Chen, S. Y. Chuang, C. H. Lin, and Y. H. Lin, "Using colloidal lithography to fabricate and optimize sub-wavelength pyramidal and honeycomb structures in solar cells," Opt. Express 15, 14793-14803 (2007).

[44]. Paddon, P., Bernhard, M. (2008). Enabling solar cells – Virtual prototyping of nanostructures. Optical engineering, Laser+Photonics

[45]. Deshpande, Ketan, "Simulation and implementation of moth-eye structures as a broadband anti-reflective layer" (2013). Thesis. Rochester Institute of Technology.

[46]. Xie, G., Zhang, G., Lin, F., Zhang, J., Liu, Z., & Mu, S. (2008). The fabrication of subwavelength anti-reflective nanostructures using a bio-template. Nanotechnology, 19(9).

[47]. Raut, H. K., Ganesh, V. A., Nair, A. S., & Ramakrishna, S. (2011). Anti-reflective coatings: A critical, in-depth review. *Energy and Environmental Science*, *4*(10), 3779–3804.

[48]. Kaltenbrunner, M., White, M. S., Głowacki, E. D., Sekitani, T., Someya, T., Sariciftci, N. S., & Bauer, S. (2012). Ultrathin and lightweight organic solar cells with high flexibility. Nature Communications, 3.